3-24-2016

Population Density Measurements of the Excited States of an Optically Excited Argon Discharge Using Emission and Absorption Spectroscopy

Steven A. Owens

Recommended Citation

Owens, Steven A., "Population Density Measurements of the Excited States of an Optically Excited Argon Discharge Using Emission and Absorption Spectroscopy" (2016). *Theses and Dissertations*. 345.
https://scholar.afit.edu/etd/345

POPULATION OF THE EXCITED STATES OF AN OPTICALLY EXCITED ARGON DISCHARGE USING EMISSION AND ABSORPTION SPECTROSCOPY

THESIS

Steven A. Owens, 2nd Lieutenant, USAF

AFIT-ENP-MS-16-M-078

DEPARTMENT OF THE AIR FORCE
AIR UNIVERSITY

AIR FORCE INSTITUTE OF TECHNOLOGY

Wright-Patterson Air Force Base, Ohio

AFIT-ENP-16-M-078

POPULATION OF THE EXCITED STATES OF AN OPTICALLY EXCITED ARGON DISCHARGE USING EMISSION AND ABSORPTION SPECTROSCOPY

THESIS

Presented to the Faculty

Department of Engineering Physics

Graduate School of Engineering and Management

Air Force Institute of Technology

Air University

Air Education and Training Command

In Partial Fulfillment of the Requirements for the

Degree of Master of Science in Engineering Physics

Steven A. Owens, BS

2nd Lieutenant, USAF

March 2016

DISTRIBUTION STATEMENT A.
APPROVED FOR PUBLIC RELEASE; DISTRIBUTION UNLIMITED.

AFIT-ENP-16-M-078

POPULATION OF THE EXCITED STATES OF AN OPTICALLY EXCITED ARGON DISCHARGE USING EMISSION AND ABSORPTION SPECTROSCOPY

Steven A. Owens, BS

2nd Lieutenant, USAF

Committee Membership:

Dr. Glen P. Perram
Chair

Dr. Robert D. Loper
Member

Dr. Christopher A. Rice
Member

Dr. David E. Weeks
Member

AFIT-ENP-16-M-078

Abstract

The populations of the excited argon $3s^23p^54s$ (s5 only) and $3s^23p^54p$ configurations in a 10 W radio frequency discharge has been studied using optical emission and diode laser absorption spectroscopy. By optically bleaching the s5→p9 transition with a narrow band laser pump of about 10 W/cm^2 at 811 nm, the p9 population was increased by about a factor of 2 at a pressure of 5 Torr. At higher pressure, collisional mixing to adjacent p-states limited the laser-increased p9 population to less than 10 percent. All other laser-induced p-state populations were minimally affected at low pressure and increased by about a factor of 4 at higher pressure. The low pressure absorption line shapes exhibited an inhomogeneous hole with band-integrated absorbance that scaled linearly with pump power. The s5 population was greater than 7×10^{11} cm^{-3} at a pressure of 5 Torr, and about 57 percent of this population was moved to the p9 state at 828 mW, or about 10 W/cm^2. Implications for development of a higher power optically pumped rare gas laser are discussed.

Acknowledgments

I would like to thank the people who helped me along the arduous rode of completing a thesis. First, I'd like to thank Dr. Glen Perram for his guidance and knowledge throughout this process, but also for introducing me to the field of directed energy. I'd also like to thank Dr. Christopher Rice and Mr. Ben Eshel for the use of and all of their assistance in their laboratory, and for their help in analysis. Mr. Greg Smith and Mr. Mike Ranft deserve thanks as well for their assistance in the laboratory.

Steven A. Owens

Table of Contents

Page

Page

List of Figures

Page

Page

List of Tables

POPULATION OF THE EXCITED STATES OF AN OPTICALLY EXCITED ARGON DISCHARGE USING EMISSION AND ABSORPTION SPECTROSCOPY

I. Introduction

1.1 Motivation for the Rare Gas Laser

Since the creation of the first high power (1 kW or above) gas lasers in the 1970s, the United States Air Force has been interested in using directed energy for both tactical and strategic purposes. As chemical lasers were developed to exceed 1 MW of output power, the Air Force shifted its interest towards chemical laser systems. Two major problems with these chemical lasers were their size and their use and production of dangerous chemicals. The most recent example outlining these issues was the Chemical Oxygen Iodine Laser (COIL) which required the use of chlorine gas and required a modified Boeing 747-400 as a platform [1]. The introduction of the diode pumped alkali laser (DPAL) by Dr. William Krupke in 2003, and their continued research and development as high power laser systems, allowed the Air Force to move their focus away from chemical lasers [2,3]. As of 2016, the highest power DPAL laser is a 1.5 kW potassium system [4].

The main scientific component of the DPAL is a three-leveled alkali vapor laser optically pumped by a diode. By using an optically narrow pump source, the transition from the ground state to the upper excited state can be well controlled so that the only optically excited state is the desired upper excited state. The upper excited state is then depopulated via optical or collisional relaxation to a specific lower excited state from which stimulated optical emission will occur, as shown in Figure 1. Unfortunately, the relative simplicity of the underlying physics for which this technology was originally chosen has become overshadowed by the complexities in engineering larger DPAL systems.

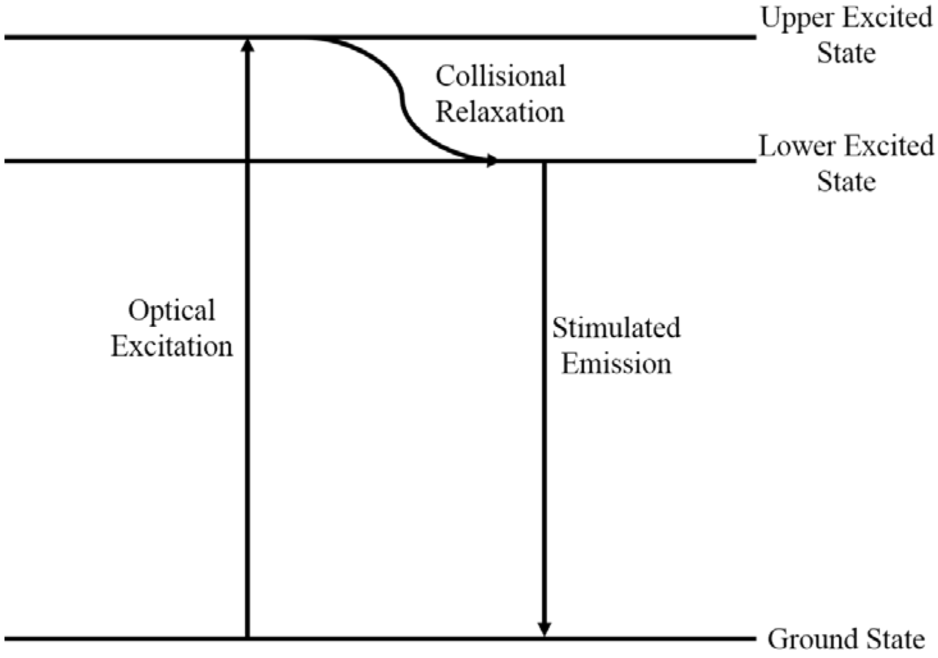

Figure 1. The three basic energy levels of a DPAL. An atom is optically excited from the ground state, collisionally relaxed to a lower excited state, and undergoes stimulated emission back to the ground state.

In most DPAL systems, a helium buffer gas is introduced to increase the spectral overlap between the pumping laser and the gain medium and to increase the relaxation rate from the upper excited state to the lower excited state. The high helium pressure required may negatively affect beam quality and increases system weight. To work around this issue, a small-hydrocarbon buffer gas, usually methane or ethane, may be introduced as well [5]. Unfortunately, alkali vapors and hydrocarbons react to form hydrides (‘laser snow’) and carbonaceous deposits on the gain cell windows (when subjected to intense light) that decrease beam quality and quench the laser [6]. This, coupled with the overall high reactivity of the alkalis, has made alkali vapor control a challenge. Thermal control inside the alkali vapor cell can also be an issue for large systems. A possible solution is to constantly flow alkali vapor through the gain cavity. The use of gas curtains has also been proposed, but no extensive testing has been done at the time of writing [5].

Because of these issues, an analogous alternative to the DPAL was sought. The analogous system would need to follow a similar optical excitation-relaxation path to the DPAL and avoid the reactivity issues. It was shown that the rare gases, also known as noble gases, in the first excited state fulfill this requirement well [5]. Rare gases in the first excited state and the alkalis both have one valence electron and can follow similar optical excitation-relaxation-emission, or laser cycle, paths. The benefit of using a rare gas over alkali vapor as a lasing medium is that it does not react in the ground state. This means the rare gases can be more easily transported and will not form hydrides. For these reasons, the rare gas laser (RGL) was chosen for further development. Argon was selected as the rare gas to use because it is relatively inexpensive and has a less complex energy level structure than heavier rare gas atoms.

While the RGL is believed to solve many of the engineering issues inherent to the DPAL system, the science behind it is more challenging. This is most apparent when looking at the differences in their respective energy level diagrams. Constructing a diagram similar to the DPAL diagram in Fig. 1 for argon requires fourteen energy levels. Many of the excited energy states are close together allowing for greater movement of population between those states at high pressure, effectively decreasing the population in the desired state, as discussed in Section 1.2. The quantum efficiency of an argon RGL is also lower than that of the DPAL, 0.89 versus 0.98 for the rubidium system. If a large-volume RGL system is proven to be viable, it could replace the DPAL as the main Air Force high power directed energy system.

1.2 Argon Rare Gas Laser Background

Because the argon atom is the only atom under consideration, all references to an atom or gas is assumed to be argon unless otherwise noted. For reference, the first fourteen excited states of argon are shown in Figure 2. On the left side of the figure, the optically allowed transitions between the p-states and s-states are shown. The energy, the angular momentum (*J*), and the Paschen notation of each state are given on the right [7].

Argon in the ground state, or s1 in Paschen notation, is non-reactive because all occupied electron orbitals are completely filled. This lack of reactivity in the ground state that makes the RGL so appealing also presents the first scientific problem. According to the National Institute of Standards and Technology, the energy difference between s1 and the lowest excited state, s5, is 11.54825 eV and, according to the transition selection rules, this transition is not electric dipole, or optically, allowed [7]. The energy difference to the second lowest excited state, s4, is 11.62359 eV and is electric dipole allowed [7]. An electron must be sufficiently excited to overcome this energy barrier so that the RGL can use the same laser cycle as the DPAL. While using a transition that is electric dipole allowed is typical in DPAL systems, the nature of the RGL actually favors one that is not. To see why this is, the dipole allowed transition (s1→s4) will be looked at first.

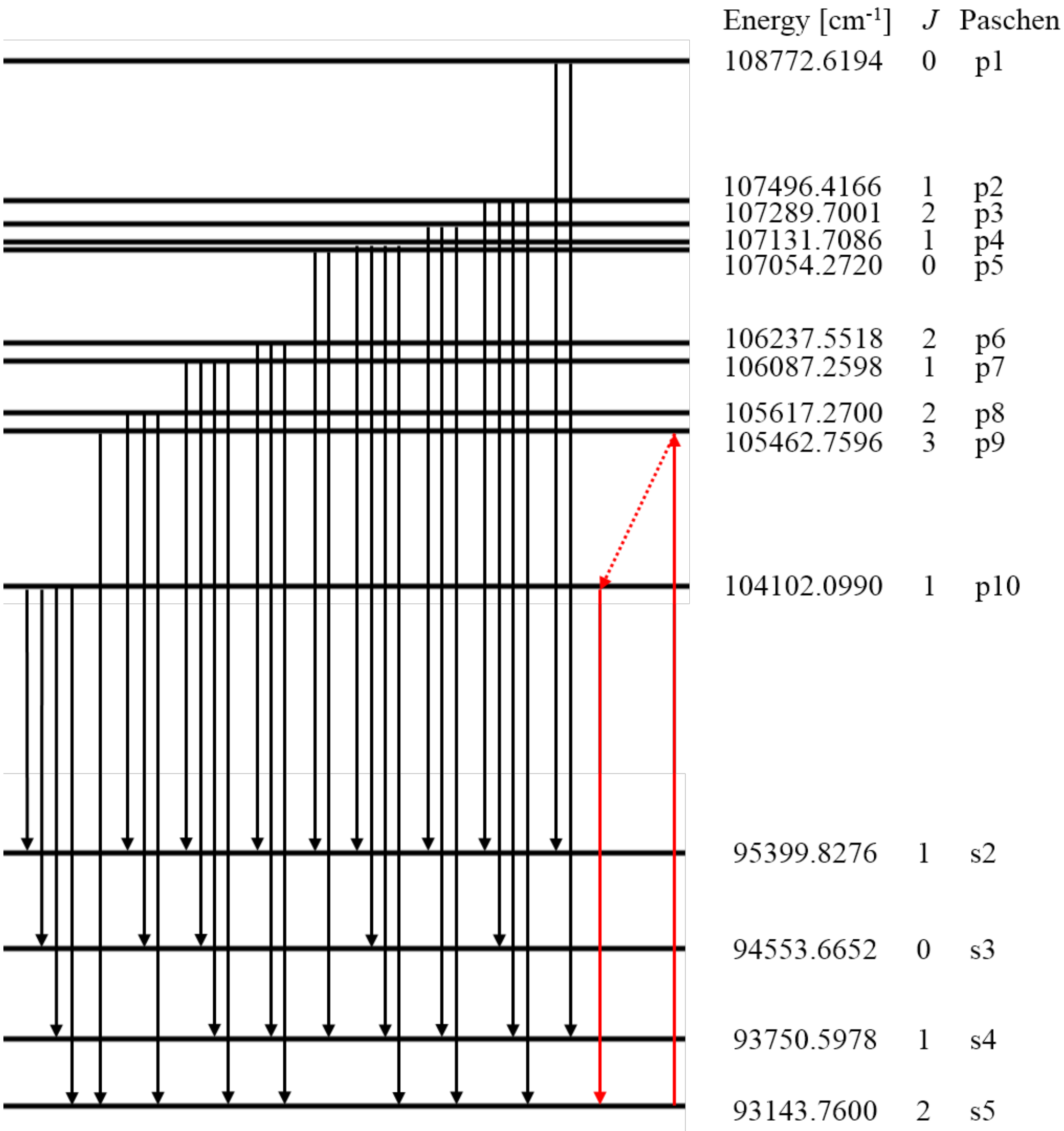

Figure 2. The first fourteen excited states of the argon atom. The optically allowed transitions between the excited states are given on the left, and the energy in wavenumbers, the angular momentum (*J*), and the Paschen notation of each state is given on the right. The proposed laser cycle of the rare gas laser is shown in red.

While using an optically allowed transition would indeed make getting population into an excited state of argon easier, it would require a high power vacuum ultraviolet (VUV) pump laser. Lasers of this type are generally complex and one of the necessary wavelength and power was not available. The transition being optically allowed would also introduce two additional problems into the RGL, both stemming from population density. High-powered lasers typically require a large population density in the upper excited state, which forces the requirement of a large population density in the state from which the atoms are being excited from. The estimated density for an efficient, high-powered argon RGL, based on absorption cross section and degeneracy, is 10^{13} atoms per cubic centimeter. In an optically allowed transition population can relax from the excited state quickly, decreasing the population density in the excited state. This means a very high-powered VUV laser would be needed to keep the excited upper state population density high enough. Additionally, for a laser such as the RGL that is not lasing to or being pumped from the ground state to be efficient, a large number of laser cycles must be completed per atom before relaxation back to the ground state. The number of laser cycles decreases as the radiative lifetime of the state decreases, and transitions that are electric dipole allowed have shorter lifetimes than those that are not. These issues make excitation from s1 to s4 unattractive for the RGL.

The s5 state retains population much better because the transition is not electric dipole allowed. This means the radiative lifetime of the state is much longer, 38 s for s5 versus 8.4 ns for s4, and the state is said to be metastable [7,8]. The population excited into the s5 state will undergo many laser cycles before relaxation back to s1. The main issue with using this metastable state is exciting population into it. Optical excitation is not viable because, as stated earlier, the s5→s1 transition is not electric dipole allowed. A promising alternative is collisional excitation. In collisional excitation, a lighter particle is energized in some manner before colliding with, and therefore giving energy to, the particle of interest. Collisional excitation from s1 to s5 using free electrons has been shown to work on multiple occasions [6,9]. One way of producing the free electrons needed is to flow argon through a small-diameter tube and subject it to a radio frequency (RF) power source [10]. Doing so creates an argon plasma with a fair amount of population in the s5 state (among many of the other possible states). For this reason, collisional excitation using free electrons generated by an RF power source was used for this research.

With the metastable s5 state established as the pseudo-ground state, the remainder of the laser cycle was chosen. To mimic the DPAL cycle as closely as possible, the optical path was decided to begin in s5, be optically pumped to p9, collisionally relaxed to p10, then lased between p10 and s5 [5]. Even though the RGL will be pumped with an optically narrow laser, the higher-energy states cannot be ignored. Due to the relative closeness of the energy levels, spin-orbit mixing between levels must be considered, especially at pressures over 100 Torr where collisions occur more frequently.

RGL proof of concept was shown first by a research group using a pulsed discharge, then a continuous discharge at low pressure, both using an argon-helium mixture [6,11]. At the beginning of 2015, another group presented a continuous, atmospheric pressure, argon-helium discharge that allowed for continuous lasing [12]. Currently, a project is underway to develop a large-volume, continuous discharge that, if successful, could provide the necessary population density to create a 1 kW laser.

1.3 Focus of this Research

While a few projects are focused on building the first large-volume RGL, there are still many diagnostics that need to be run to better understand the dynamics of the argon plasma discharge. This research focused on the changes in population density of the p-states discussed above when an argon discharge is optically excited, and how those population densities change with discharge pressure. The information gained from this diagnostic will help determine operational parameters of a rare gas discharge and may lead to better designs of large-volume systems.

II. Theory

2.1 Optical Emission Spectroscopy

To measure the change in the p-state population densities of the argon plasma, a measurement technique called optical emission spectroscopy, or OES, was used. OES involves collecting the fluorescence emitted by atomic transitions and directing it through a spectrometer. The spectrometer will separate the fluorescence into its component wavelengths, creating a spectrum. Each wavelength will create a spectral line, and the intensity of each line is recorded. If the energy levels of the atom in question are well known, as they are for the argon atom, the wavelengths at which signal is collected can be matched to specific atomic transitions between two states. These transitions are commonly called transition lines. If the rates of spontaneous emission, or the Einstein A coefficients, and the degeneracy of transition lines are known, then the population of the excited states can be related to the collected intensity by

$$I_{ji} \propto A_j n_j \propto A_{ji} g_j e^{-\frac{\Delta E}{k_B T}} \tag{1}$$

where I_{ji} is the intensity associated with the transition from the excited state j to the lower state i, A_{ji} is the Einstein A coefficient of the transition, g_j is the degeneracy of the excited state, ΔE is the energy difference between state j and the ground state, k_B is Boltzmann’s constant, and T is the temperature of the gas. Equation (1) can be rewritten as

$$\ln\left(n_j\right) \propto \ln\left(\frac{I_{ij}}{A_{ji} g_j}\right) \tag{2}$$

and the $\ln(n_j)$ term on the left hand side is taken as the effective population of the upper state. It is important to note that Equation (2) is only valid if the absorbing medium is optically thin and in equilibrium, which may not be the case for the argon plasma generated during this experiment.

To accomplish the objectives of this research, the fluorescence of an argon plasma discharge generated inside of a tube was viewed from the side. As the argon discharge is optically excited, or pumped, the amount of population in the excited states should increase for all transitions. The effect of pressure is much less predictable. As pressure increases, the density of atoms available to be excited increases and spin-orbit mixing between states becomes a larger factor. The argon discharge changes from a uniform, stable plasma at low pressure (less than 400 Torr) to a non-uniform, unstable plasma at higher pressures. The increasing argon density also means the discharge is optically thicker at high pressures than at low pressures, which could inhibit excitation and lead to radiation trapping. If radiation trapping is a significant factor, the peaks of the observed spectral lines will be shorter than if no trapping was present.

This measurement technique is most powerful in the bleached domain. In the bleached domain, the maximum amount of population that can be moved into an excited state is optically excited into the excited state and the laser power that isn’t used passes through the discharge relatively unaffected. It was believed a focusing optic would be needed to reach the bleached regime of the argon plasma with the pump laser available. While a shorter focal length lens will result in a spot with a smaller diameter and greater intensity, it will also lead to a greater beam divergence which decreases the volume of the discharge that is over the bleached limit. An appropriate balance between these two parameters was attempted.

OES is limited by transitions lines that emit enough photons to be distinguished from detector noise. The amount of emission from a transition line, called the strength of the transition, is dependent on factors such as emission cross section and density of the upper transition state, but the Einstein A coefficient is typically a good indicator because it indicates how quickly population in an excited state will undergo optical relaxation. Using these coefficients as a starting point, and with the limitations of the spectrometer that was to be used, the transition lines listed in Table 1 were chosen for analysis.

Table 1. Investigated Transitions for OES Experiment

Vacuum Wavelength (nm)	A_{ji} (10^6 s^{-1})	E_i (cm^{-1})	E_j (cm^{-1})	Lower State, i		Excited State, j	
				J	Paschen Notation	J	Paschen Notation
750.5935	44.5	95 399.8276	108 722.6194	1	s2	0	p1
696.7352	6.39	93 143.7600	107 496.4166	2	s5	1	p2
727.494	1.83	93 750.5978	107 496.4166	1	s4	1	p2
772.6333	11.7	94 553.6652	107 496.4166	0	s3	1	p2
826.6794	15.3	95 399.8276	107 496.4166	1	s2	1	p2
706.9167	3.80	93 143.7600	107 289.7001	2	s5	2	p3
738.6014	8.47	93 750.5978	107 289.7001	1	s4	2	p3
841.0521	22.3	95 399.8276	107 289.7001	1	s2	2	p3
795.0362	18.6	94 553.6652	107 131.7086	0	s3	1	p4
751.6721	40.2	93 750.5978	107 054.2720	1	s4	0	p5
763.7208	24.5	93 143.7600	106 237.5518	2	s5	2	p6
800.8359	4.90	93 750.5978	106 237.5518	1	s4	2	p6
772.5887	5.18	93 143.7600	106 087.2598	2	s5	1	p7
810.5921	25.0	93 750.5978	106 087.2598	1	s4	1	p7
801.699	9.28	93 143.7600	105 617.2700	2	s5	2	p8
842.6963	21.5	93 750.5978	105 617.2700	1	s4	2	p8
811.7542	33.1	93 143.7600	105 462.7596	2	s5	3	p9

All of the excited s-states and nine of the ten p-states are represented in Table 1 [7]. The p10 state was not able to be measured because all of the p10 transitions occurred at longer wavelengths than the spectrometer grating motor could rotate the grating to accommodate. The transitions are usually referred to by the general wavelength corresponding to the energy difference between the states. For example, the s5→p9 transition is called the 811 nm transition or line. This notation is followed throughout this thesis.

2.2 Tunable Diode Laser Absorption Spectroscopy

To find the absolute densities in the excited states, tunable diode laser absorption spectroscopy, or TDLAS, was used. To find the density of the excited states with TDLAS, two lasers are needed. One laser is used to pump the argon discharge and the other, commonly called the probe laser, scans over a wavelength range that includes a different transition line that uses the same pseudo-ground state (s-state) as the pumping transition. As the probe laser scans over its transition, some of the probe laser is absorbed by the atoms in the plasma. As pump laser power increases, the amount of probe laser absorbed decreases because there are fewer atoms in the pseudo-ground state. If the power of the probe laser is measured before and after the plasma, this absorption can be quantified by taking the natural log of the ratio of the powers. If the area of the detectors can be assumed equal, the absorbance, A, can be defined as

$$A = -\ln\left(\frac{I}{I_0}\right) = \sigma\left(\upsilon_{ij}\right) n_i \, l \tag{3}$$

where I is the intensity measured after the plasma, I_0 is the intensity measured before the plasma, $\sigma(\upsilon_{ij})$ is the frequency-dependent absorption cross section of the transition, n_i is the density in the excited state, and l is the length of the medium through which the probe laser propagates. Rearranging to solve for density,

$$n_i = \frac{1}{\sigma\left(\upsilon_{ij}\right) l} A. \tag{4}$$

The intensity of the probe beam inside the discharge should be low enough that it does not significantly affect the discharge itself.

2.3 Lamb-Dip Absorption Profile

In an ideal world, the profile of each transition, or lineshape, would be a straight, vertical line resembling a delta function located at the wavelength corresponding to the energy difference between the upper and lower states. But, due to the uncertainty principle, the Doppler effect, and pressure, real lineshapes will always have a finite width. The width and shape of each spectral line is determined by which form of broadening is dominant, either homogeneous, also known as Lorentzian, which affects the lineshape uniformly or inhomogeneous, also known as Gaussian, which only affects certain parts of the lineshape. Lorentzian broadening is typically associated with the uncertainty principle and pressure, and typically dominates the lineshape at higher pressures. Inhomogeneous broadening is generally dominated by the Doppler effect and will be referred to interchangeably with Doppler broadening as a result. Doppler broadening dominates the lineshape at low pressure. Completely Lorentzian or Doppler lineshapes can be useful approximations, but a more accurate description of the lineshape is a combination of both pieces to form what is called a Voigt profile. A Voigt profile includes the behaviors of both lineshapes when neither broadening is dominant and will reduce to the dominant broadening appropriately.

While a Voigt profile is sufficient to describe many transition lineshapes, specific circumstances require more complex lineshapes. One such circumstance is the use of multiple lasers as described in Section 2.2. At low pressures the lineshape will be Doppler broadened, but the introduction of a second laser causes a Lorentzian dip in the lineshape, called a Bennet hole, if the probe laser scans over the same velocity group being depleted by the pump laser. As pump laser power increases, the Bennet hole increases in depth and width and decreases the height of the Doppler lineshape as a whole. If the pump and probe beams are at the same wavelength, the Bennet hole is called a Lamb dip and occurs at the center of the lineshape. If two different wavelengths are used for the pump and probe beams, this effect can be produced if both wavelengths correspond to transitions with the same lower energy state. As long as the probe laser is significantly weaker than the pump laser such that it does not affect the medium under investigation, the lineshape is described by

$$g_s(\omega) = g^0(\omega) \frac{\Delta\upsilon_H/2}{B\left[1-\left(\frac{2(\omega-\omega_0)}{A+B}\right)^2\right]^{1/2}} \tag{5}$$

$$A = \left[(\omega-\omega_0)^2 + (\Delta\upsilon_H/2)^2\right]^{1/2} \tag{6}$$

$$B = \left[(\omega-\omega_0)^2 + (\Delta\upsilon_H/2)^2\left(1+2\frac{I}{I_S}\right)\right]^{1/2} \tag{7}$$

where $g_s(\omega)$ is the saturated absorption lineshape, $g^0(\omega)$ is the unsaturated absorption lineshape, $\Delta\upsilon_H$ is the unsaturated homogeneous linewidth, ω is the radial frequency of the probe laser, ω_0 is the center radial frequency of the transition, I is the pump laser intensity, and I_s is the saturation intensity of the medium [13]. The unsaturated absorption lineshape is

$$g^0\left(\omega\right) = \Delta N_0 \frac{\sigma\left(\omega_{ij}\right)\Delta\upsilon_H\, c\sqrt{\pi}}{\nu_p\, \omega} \tag{8}$$

$$\Delta N_0 = N_u^0 - \frac{g_u}{g_l} N_l^0 \tag{9}$$

where ΔN_0 is the unsaturated population difference, c is the speed of light, v_p is the most probable velocity as defined by statistical mechanics, g_u is the upper energy state degeneracy, g_l is the lower energy state degeneracy, N_u^0 is the population density in the upper state with no pumping, and N_l^0 is the population density in the lower state with no pumping [13]. By performing a linear least-squares fit on data with a Lamb dip lineshape, the amount of population moved between two energy states can be found. Even if the Lamb dip is not obvious when looking at the lineshape, Equations 5-9 are still valid because they correspond to the measurement technique used.

III. Experiment

3.1 Setup for Optical Emission Spectroscopy

The optical emission spectroscopy experiment was set up as shown in Figure 3. A Coherent V-18 neodymium-doped yttrium lithium fluoride (Nd:YLF) diode pumped laser with a maximum output of 18 W and a wavelength of 532 nm with a 5 MHz linewidth was used to pump a Spectra Physics Matisse TX, a scanning titanium-sapphire (Ti:Si) rign laser. The Matisse TX setup used for this experiment had a wavelength tuning range from 750 nm to 870 nm, a scanning range of 30 GHz, and a laser linewidth of 30 kHz. This narrow linewidth was achieved because the Matisse TX used a reference cell as part of a feedback loop to measure the wavelength of the laser output and correct the laser cavity appropriately. After passing through the reference cell, the beam passed through a 2 in. diameter glass beamsplitter. The beam reflected off of the glass was directed to a High Finesse Angstrom WSU2 Wavelength Meter and was used to monitor the wavelength of the Ti:Si output laser to an accuracy of 5 MHz. The transmitted beam passed through a Thorlabs GBE05-B, an AR coated (650-1050 nm optimized), 5-times achromatic Galilean beam expander. Expanding the beam in this manner changed the behavior of the beam from divergent to convergent, causing the spot size to be focused down on the test cell side of the setup. This was necessary because the smallest spot size possible was desired inside the test cell. The beam was then directed through a Thorlabs reflective neutral density (ND) filter set and into the test cell. The ND filters were used to adjust the pump laser power without directly changing the power output of the Matisse TX due to repeatability concerns. The test cell was housed inside a grounded Faraday cage to prevent the radio-frequency (RF) power source used to create the plasma discharge from interfering with any of the electronics used for the various measurements required to complete this experiment. Overall, the Matisse TX beam traveled 8.496 m and was reflected by nine surfaces before entering the Faraday cage, causing the power of the beam entering the Faraday cage to be about 30% lower than the power measured at the reference cell exit aperture. In an effort for clarity, any reference to the pump beam will correspond to the Matisse TX beam as it enters the Faraday cage.

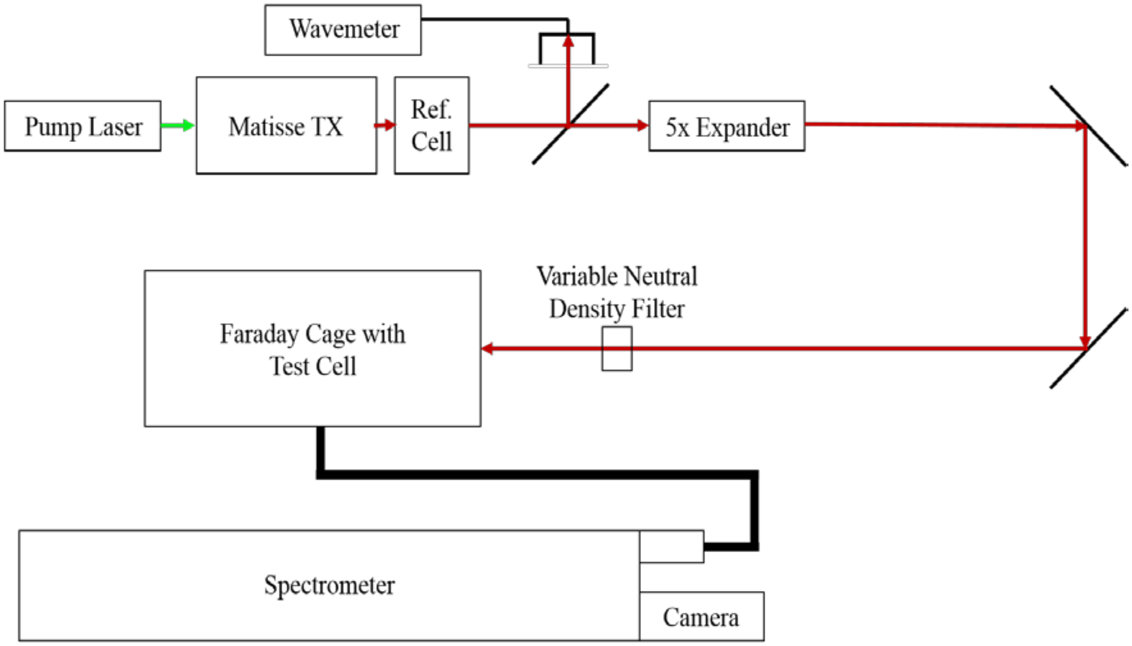

Figure 3. Experimental setup used for OES measurements, outside of the test cell. All computers and lock-in amplifiers are omitted to increase visual clarity.

The test cell inside the Faraday cage was set up as shown in Figure 4. The test cell itself was constructed by connecting a wedge window flange, a zero-length A&N CF double-sided flange to female national pipe thread (NPT) with side port, and an A&N quick connect fitting to CF flange hybrid adapter to one another, in that order, with silver-coated copper gaskets in between each piece. Two of these devices were made. A 6.28 mm outer diameter, 3.89mm inner diameter Pyrex tube was fitted with a rubber o-ring, inserted into one of the hybrid adapters, and secured. The plasma-generating voltage system, comprised of a high voltage cable, a ground cable, and two aluminum electrodes epoxied to a 15.4 mm ceramic spacer, was then slid onto the Pyrex tube. The high voltage cable was connected to a Dressler Cesar Generator model 1310, a 13.56 MHz radio frequency (RF) power supply with an impedance matching network. For all experimental measurements, the RF power supply configured so that the power delivered to the test cell was 10 W and the reversed power was less than 1 W. The ground cable was secured to the laboratory table, which was also grounded. The size of the hole in the aluminum brackets through which the Pyrex tube went through was slightly larger than the tube itself. This allowed the plasma discharge to be moved in the direction of beam propagation as needed. The open end of the Pyrex tube was fitted with a rubber o-ring and secured to the second flange-adapter device. The entire system had an argon leak rate of less than one Torr per hour. To view the plasma created inside the test cell, a multi-mode, eighteen core optical fiber was used. Each core was 0.33 mm in diameter and had a numerical aperture of 0.22 with a 0.02 uncertainty. The fiber used had an entrance ferrule with all of the fibers bundled into a circle. This end was placed one focal length away from a 1/2 in. focusing lens inside of a metal housing. The exit ferrule of the fiber arranged the cores into a line. This type of fiber was used because it generated the greatest amount of vertical distribution on the detector, which increased the resolution of the fiber-spectrometer system. A vertical line orientation also ensures the diffraction patterns of the light entering the spectrometer do not interfere with one another in a way that would distort the data.

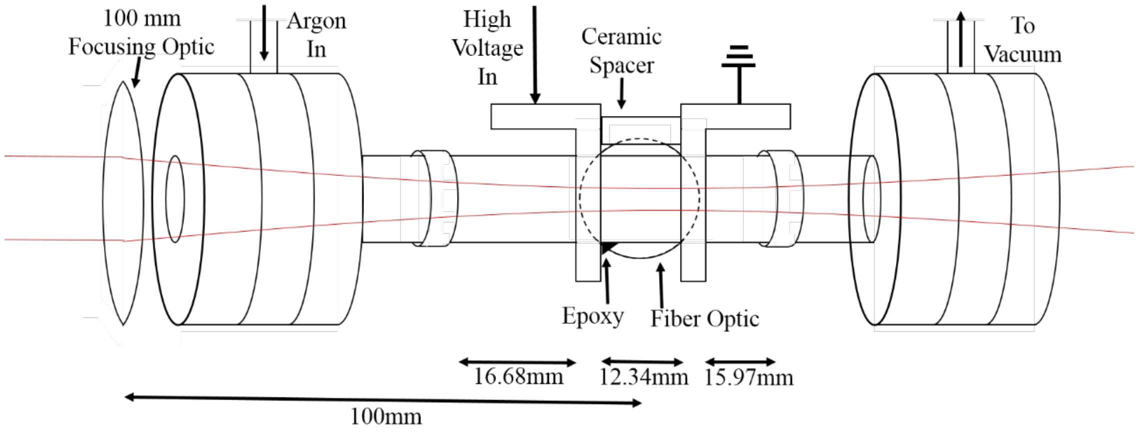

Figure 4. Setup of the test cell used for OES measurements.

The fiber housing was then mounted onto a three-dimensional translation stage. Placement of the optical fiber was taken under great consideration as a balance between the stability of the discharge within the viewing volume and the amount of signal collected had to be found. The discharge between the two electrodes filled the Pyrex tube in a non-uniform fashion when the pressure inside the test cell was raised over 300 Torr. This behavior is shown in Figure 5. With the pressure inside the test cell set at 5 Torr, the argon discharge filled the entire Pyrex tube and appeared optically thin. As pressure increased, the discharge became concentrated into a plasma column, physically moved upward, and shortened. At a test cell pressures of 400 Torr and 700 Torr, the discharge formed two plasma columns, one very strong column and one wispy column. The plasma column at 700 Torr filled about one quarter of the volume filled by the plasma at 5 Torr. When the plasma was viewed at a rate of 10 kHz, another homogeneity problem arose. At 5 Torr the plasma was not a homogeneous column at all, but instead distinct plasma striations that flowed through the entire tube after the first electrode. The distinctness of the plasma striations decreased with pressure and only occurred after the second electrode at pressure of 100 Torr and 400 Torr. No striations in the 700 Torr case were observed, but the plasma column oscillated between the electrodes.

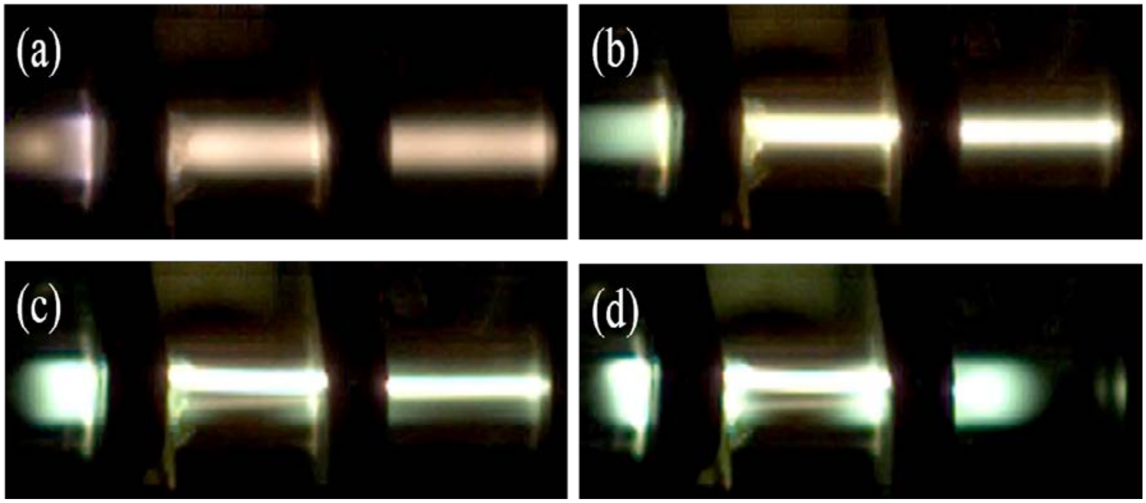

Figure 5. The argon discharge inside the test cell at a pressure of (a) 5 Torr, (b) 100 Torr, (c) 400 Torr, and d) 700 Torr

The non-uniformity and changes in position of the discharge as pressure increased posed a major problem. When the discharge moved upward, it began to move out of the focused pump laser spot and the volume viewable by the fiber optic. This means less of the viewed volume was being pumped than expected. It was also found that the throughput of the fiber changed as a function of individual fiber position, as shown in Figure 6. The viewing volume had a maximum diameter of about 1000 µm and the viewing volume diameter for each component fiber, or one peak on the plot, was only about 200 µm. The plot also shows that some of the fibers had a much better throughput signal than others. So, if the discharge was only illuminating a few fiber cores, as occurred at higher pressure, the intensity throughput would have been dependent upon which specific fibers were being illuminated. In addition to this issue, the discharge between the electrodes was also unstable at test cell pressures of 400 Torr and above. At a pressure of 700 Torr, the period of oscillation of the discharge was on the same order as or less than the 100 ms integration time used during data acquisition.

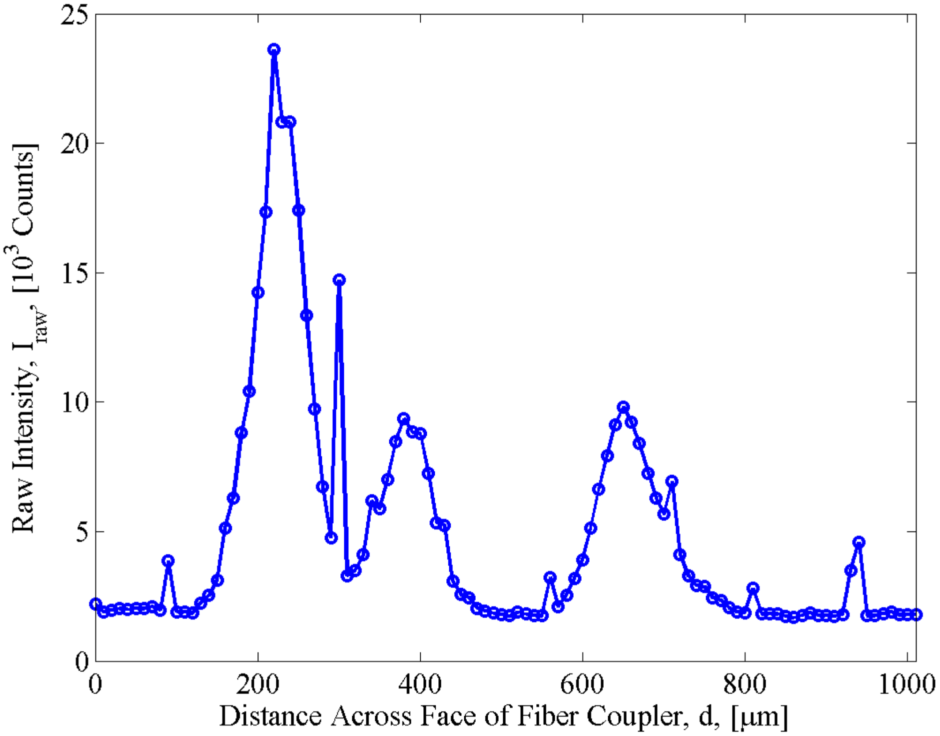

Figure 6. The spatial response curve of the fiber optic along one dimension across the face of the fiber. Solid lines were used with the data points to increase clarity.

The discharge after the second electrode also presented issues. While the discharge at this position was stable at all pressures, the strength of emission at this position weakened as pressure increased. At a pressure of 700 Torr, very little, if any, signal could be seen above the detector noise for all lines because of the short distance that the discharge extended past the second electrode. Because distinguishable signal was crucial for this experiment, the fiber was positioned to view the discharge between the two electrodes with the understanding that a greater amount of error would be introduced into the data. The front of the fiber optic was then positioned so that the focusing lens inside the housing was 19 mm away from the center of the discharge. Then, the fiber position was adjusted slightly with the translation stage to maximize the signal throughput.

Ultra-high purity (99.999%) argon was used in all experiments. From the tank, the argon passed through 1/4 in. stainless steel pipes to a Sierra SmartTrak 50 mass flow controller set at 100 sccm. It was then directed, using 1/4 in. stainless steel pipes, through a MicroTorr model MC200-904FV filter to increase the argon purity to research grade (99.9999%) and an MKS Baratron Type 690A absolute pressure sensor to measure the pressure before, or upstream of, the test cell. The pressure was displayed on an MKS Type 670B high accuracy signal conditioner. From the Baratron, a flexible plastic tube was used to deliver the argon into the test cell via a 1/4 in. Swagelock-to-1/16 in. NPT connection to the zero-length A&N flange mentioned above. To create an argon flow and to control the pressure of argon inside the test cell, a vacuum line was added. The vacuum line mirrored the argon delivery system from the Baratron to the cell, but on the opposite zero-length A&N flange. The vacuum side Baratron was used to measure the pressure on the downstream side of the test cell, and that pressure was displayed on an MKS Controller as well. From the Baratron, 1/4 in. stainless steel pipe was used to direct the flow through a butterfly valve and into the vacuum pump. The butterfly valve was controlled by an MKS 600 series pressure controller. The MKS 600 controller was used to regulate the pressure inside the test cell by opening and closing the butterfly valve appropriately as part of a proportional–integral–derivative (PID) loop. Pressures of 5

Torr, 100 Torr, 400 Torr, and 700 Torr were used in this study. At 100 sccm, these pressures corresponded to flow velocities of 33.9 m/s, 1.69 m/s, 0.42 m/s, and 0.24 m/s and dwell times of 0.0133 s, 0.2655 s, 1.0621 s, and 1.8587 s, respectively.

A focusing optic was placed in front of the test cell so that the focus of the beam would be within the test cell. In this experiment, a highly-focused beam was desired, so a 100 mm focal length, 1in. calcium-fluoride plano-convex lens was chosen as the focusing optic because calcium-fluoride allows over 90% transmission at the wavelengths under consideration and a plano-convex lens introduces only a small amount of spherical aberration. This focal length determined the placement of the electrodes and fiber housing, i.e. 100 mm away from the lens. At this distance from the lens, the electrodes were held in place by a dab of high temperature (150° C) epoxy placed so that it would not be within the viewing volume of the fiber optic.

Light emitted from the plasma discharge was collected by the fiber and passed to a McPherson Model 209, 1.33 m Czerny-Turner scanning spectrometer. The spectrometer was configured so that the rectangular end of the fiber optic faced an entrance slit with a changeable width. Light that made it through the fiber would pass from the rectangular end of the fiber and impinge upon the entrance slit, which was set at 100 µm wide, resulting in a diffraction pattern. The diffraction pattern reflected off of a collimating mirror onto an 1800 grating/mm, magnesium-fluoride coated, holographic diffraction grating. The diffraction grating split the collimated light into the component wavelengths, which then reflected off of a focusing mirror onto the 1024-by-1024 pixel, intensified charge-coupled device (iCCD) array of a Princeton Instruments PI-MAX2 camera system that had a 26 µm pixel pitch. The image formed on the array was displayed on a computer using the Princeton Instruments WinView/32 software, where it could be further manipulated and analyzed.

3.2 Calibration of PI-MAX2 Camera System

To ensure the data gathered were accurate, the spectrometer was aligned and calibrated. The first step was to align the input of the spectrometer with the output. The internal mirrors and grating of the spectrometer were positioned so that the zeroth order bright fringe of the diffraction pattern of a Uniphase 1676 helium-neon (HeNe) laser passing though the entrance slit was centered on each reflective surface. A vertical stop on the entrance slit of the spectrometer was adjusted to the smallest setting so that the diffraction spot was as vertically small as possible. The reflective surfaces inside the spectrometer were again adjusted until the spectral line of the HeNe was vertically centered on the PI-MAX iCCD. The entrance slit of the spectrometer was calibrated as detailed in Appendix A. The throughput of the fiber optic was then optimized by adjusting the position of the rectangular end of the fiber until the intensity on the PI-MAX iCCD was maximized and the lineshape of the spectral line was symmetric. Intensity calibration of the PI-MAX iCCD was accomplished by comparing an experimentally gathered spectrum from an Oriel Instruments 200 Watt quartz tungsten halogen (QTH) lamp with a calibration spectrum provided by Oriel Instruments. This process is shown in detail in Appendix B.

3.3 Data Acquisition for Optical Emission Spectroscopy

The first step of data acquisition was to experimentally find the intensity curves as a function of pump laser power for the 811 nm line for each pressure to be used in the later experiments. After ensuring the scatter from the Matisse TX laser would not significantly influence any data, the Matisse TX was tuned to the 811 nm transition line and the output power directly after the reference cell was recorded. The pressure inside the cell was then set to 5 Torr and the discharge was turned on. Then the spectrometer was adjusted so that the 811 nm line was near the center of the iCCD array. This was done so that any irregularities inherent to the iCCD array were avoided. Spectra of the discharge were then taken with integration times of 100 ms and with different neutral density filters in the pump laser beam path. The ND filters used ranged from optical density (OD) 0.0 to 3.0 in steps of 0.1, and a blocked pump beam data acquisition was taken both before and after using the neutral density filters. After all the necessary data were taken at a pressure of 5 Torr, the discharge was turned off and the power after the reference cell was again recorded. This process was repeated for pressures of 100 Torr, 400 Torr, and 700 Torr. The pump laser power was taken between each pressure run to ensure the laser power delivered to the test cell was decreasing due to the ND filters only, not a combination of laser cavity fluctuations and ND filters. If the power measured after the reference cell was within 30 mW of the power measured before any data were taken, data collection continued. If the measured power had fallen below the lower bound of the acceptable range, the laser cavity was tuned so that the power was within the range and the data at the previous pressure was retaken. If the measure power had risen above the higher bound of the acceptable range, any previously acquired data was retaken. After all of the discharge-related data had been taken, the laser power delivered to the cell when using each ND filter was recorded.

After the intensity curves were found, the optical excitation spectroscopy (OES) experiment was performed. All ND filters were removed, the Matisse TX was tuned to maximum power output to ensure bleaching occurred, the pressure inside the test cell was set to 5 Torr, and the discharge was turned on. The center of the pressure-shifted 811 nm transition was then found using the same type of absorption measurement described in Section 2.2. An approximate pressure-shifted line center was calculated using a previously experimentally determined shift rate for the argon 811 nm transition of 4.26±0.39 MHz/Torr towards the red [14]. From this calculated transition line center, the Matisse TX frequency was fine-tuned until absorption of the probe laser was minimized. Frequency was used because the Wavelength Meter was accurate to more significant digits when monitoring frequency as opposed to wavelength. The spectrometer was then adjusted so that the 696 nm line was centered on the iCCD. Data were then taken, with an integration time 100 ms, when the pump laser was blocked, then unblocked. The spectrometer was subsequently adjusted so that the center of each line listed in Table 1 was centered on the iCCD, and data were taken in the blocked, then unblocked method described above. This process, including the Matisse TX frequency tuning, was then performed for pressures of 100 Torr, 400 Torr, and 700 Torr.

For every transition line presented in Table 1, six images were gathered. The first three were taken with the pump laser blocked, and the second three were taken with the pump laser going through the cell. This was done so that some amount of the fluctuations present over a short timescale in the discharge could be taken into account. For each image, five data acquisitions were taken. This WinView/32 function overlaid five separate “snapshots” of the discharge fluorescence and added them together to create one image, further taking into account short timescale discharge fluctuations. In post processing each image was divided by five before being averaged together with similar images (e.g. all of the 811 nm transition images with the pump laser blocked), which resulted in one image presenting the average emission due to a specific transition line.

3.4 Setup for Tunable Diode Laser Absorption Spectroscopy

The tunable diode laser absorption spectroscopy (TDLAS) experiment involved changing the experiment setup, as shown in Figure 7. As can be seen in the figure, a laser diode was added to the setup. The laser diode was a New Focus Velocity 6314 tunable diode laser with wavelength range of 794 nm to 804 nm, and the wavelength of the laser diode was tuned across 62.5 GHz using an Agilent model 33220A 20 MHz function/arbitrary waveform generator by driving an internal piezo to change the cavity length appropriately. The beam produced by this diode was reflected off of two mirrors before passing through a chopper wheel. A chopper wheel was used to modulate the laser diode beam so that it could be distinguished from the noise and the pump beam after the bandpass filter. The diode beam then passed through two 98/2 pellicles. The reflection from the first 92/8 pellicle was directed into a Thorlabs PDA100A Si switchable gain detector set at a 0 dB gain, and the reflection from the second 92/8 pellicle was then reflected off of a 1 in. mirror mounted on a Newport model 9891 flipper optic mount and into the Wavelength Meter. A flip mirror was installed because both the Matisse TX wavelength and the laser diode wavelength needed to be monitored. To coalign the diode laser with the Matisse TX beam, a Thorlabs PBS 252 1 in. polarizing beamsplitter cube was installed before the beam expander. The variable ND filter set was moved to directly after the reference cell because the Matisse TX was used as the pump beam described in Section 2.2.

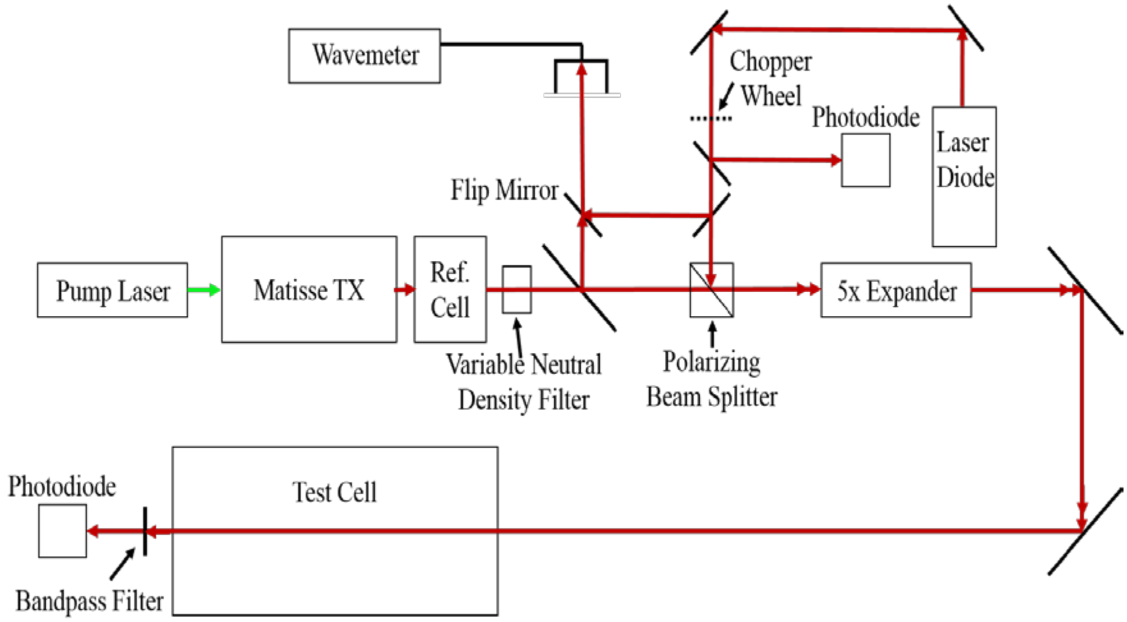

Figure 7. Setup for the TDLAS experiment. All computers and lock-in amplifiers are omitted to increase visual clarity. The path over which the pump beam (at the p9→s5 transition) and probe beam (scanning over the p8→s5 transition) were aligned is indicated with a double arrow.

Due to the different measurement technique used for TDLAS, the fiber optic and spectrometer were no longer used. Instead, the beams passing through the cell were allowed to leave the Faraday cage, pass through an Edmond Optics bandpass filter centered on 795 nm with a 10 nm full-width, half-maximum (FWHM), and into another PDA100A photodiode set to a 0 dB gain with a focusing optic fitted in front of the detecting surface. The 795 nm bandpass filter was selected because it would block out most of the pump beam (the Matisse TX) while allowing enough of the probe beam (the laser diode) through despite the probe beam not being within the FWHM of the filter. Nothing inside the test cell was changed. The two photodiodes were connected to separate Stanford Research Systems SR850 DSP lock-in amplifiers that were both set to measure the signal of the frequency-modulated probe beam. ND filters were added in front of the first photodiode so the signal on both lock-in amplifiers was as close to the same as possible when the discharge was off. This was critical for the TDLAS measurements, as the ratio of the signals needed to be as close to one as possible when no absorption was present for the results to be accurate.

3.5 Data Acquisition for Tunable Diode Laser Absorption Spectroscopy

To start the TDLAS measurements, the pressure inside the test cell was set to 5 Torr and the Matisse TX laser frequency was adjusted to the pressure-shifted lineshape center of the 811 nm transition. The flip mirror was then erected so that the wavelength meter would read the wavelength of the laser diode during scanning. To take data, the signal delivered to each photodiode due to the laser diode was recorded as the laser diode scanned over the 801nm transition. A single data run with the discharge off and the Matisse TX beam blocked was taken first so that any anomalies inherent in the diode laser and laser propagation could be removed from the data in post processing. The discharge was then turned on, and another data run was taken with the Matisse TX beam blocked (i.e. the unpumped absorption curve). The Matisse TX beam was then unblocked and a data run was taken for pump powers of 58 mW, 117 mW, 218 mW, 448 mW, and 828 mW.

IV. Analysis and Results

4.1 Fluorescence Spectrum

For every pressure and pumping condition, a spectrum like the one presented in Figure 8 was acquired. Each spectrum consisted of the corrected acquired lineshape of every transition listed in Table 1. For all cases, the s4→p2 transition, or the 727 nm line, was too weak to result in a clean lineshape. This was not too surprising as that transition has the lowest spontaneous emission coefficient of all of the lines and begins on a p-state high in the manifold. Because a clear lineshape did not exist, the 727 nm line was not analyzed. The two transition lines near 772 nm complicated analysis. While the individual lines are resolvable, the lineshapes are not independent of one another. To account for both lines individually, an artificial separation at 772.615 nm was applied in post-processing. Any data near the 772 nm lines with a wavelength shorter than 772.615 nm was assumed to be associated with the 772.5887 nm line, while any data with a wavelength longer than 772.615 nm was assumed to be associated with the 772.6333 nm line. A more accurate way to separate these lines would have been to fit the peaks with a Voigt profile to account for both homogeneous and inhomogeneous broadening and analyze the lines independently. This method was not used due to time constraints. Instead, it was reasoned that any data lost by a transition line due to the break would be added back to the lineshape with the data lost by the other transition line. While this method may not have been the most accurate way to separate the lines, it was a good enough approximation when compared to the magnitudes of the data.

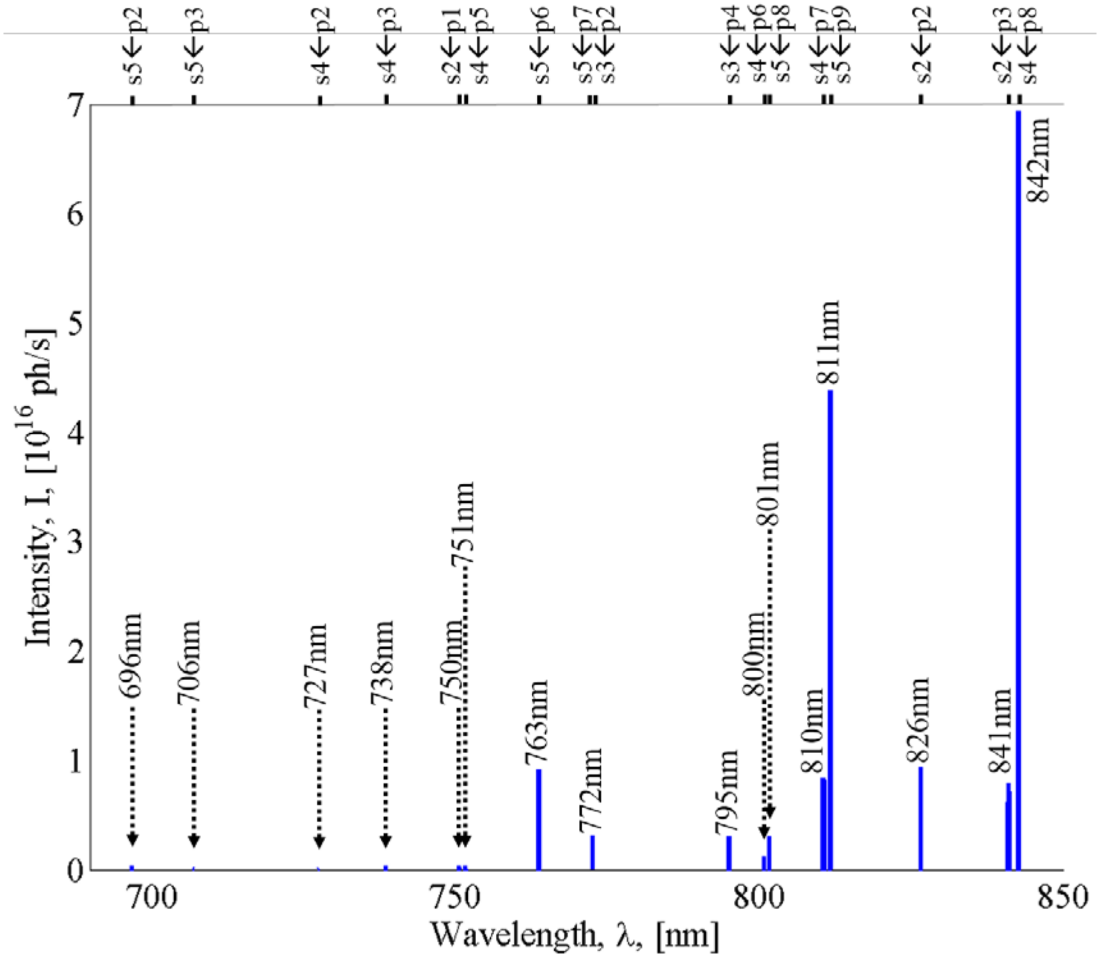

Figure 8. The full spectrum gathered for the unpumped, test cell pressure of 100 Torr case. Intensity of each transition is given as a function of wavelength. The upper and lower states of the transitions are listed across the top and the associated general wavelength is given at the location of each line.

Figure 8 appears to be a stick spectrum of the transitions under consideration, but each line actually has a lineshape associated with it. For the unpumped, test cell pressure of 100 Torr case shown in Figure 8, each transitions has a Voigt profile. This is shown in Figure 9. As can be seen, the type of lineshape does not depend on wavelength or intensity. This is consistent with theory as only pressure should significantly affect the lineshape type.

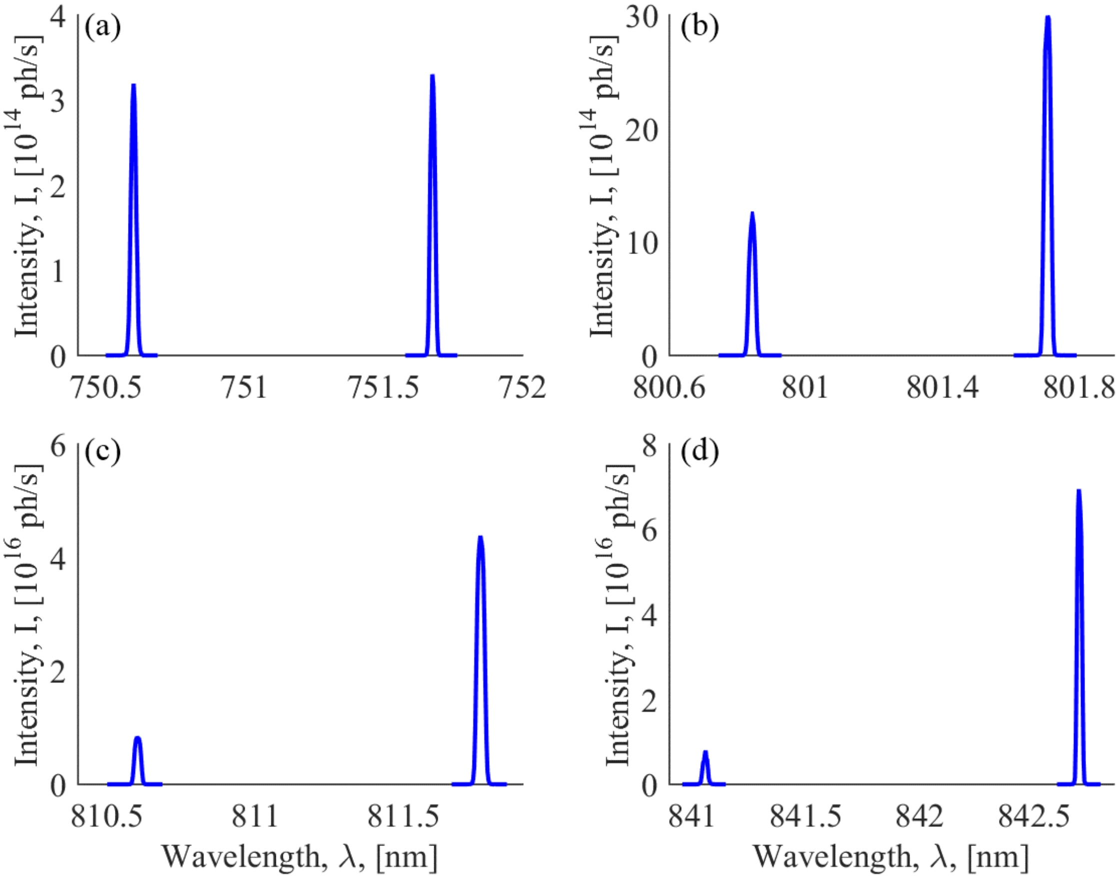

Figure 9. Four groups of lines showing the Voigt lineshape that was collected for each transition line under consideration. The specific lines shown are the (a) 750 nm and 751 nm lines, (b) 800 nm and 801 nm lines, (c) 810 nm and 811 nm lines, and (d) 841 nm and 842 nm lines. These lines were chosen so that many of the lines under consideration could be shown without including each line in an individual plot.

4.2 Bleaching Intensity Curves

Before the 811 nm bleaching curves were experimentally found, the power required for bleaching was calculated for the idealized case of the setup. One way to approximate this value is to find the intensity required to saturate the gain medium, or

$$I_b = \sigma(\upsilon) n_i \, l I_S \tag{10}$$

where I_b is the bleaching intensity, $\sigma(\upsilon)$ is the frequency-dependent absorption cross section of the transition, n_i is the population density in the lower state of the transition, l

is the length of the propagation through the gain medium, and I_s is the saturation intensity. A rule of thumb is that the bleaching intensity is ten times greater than the saturation intensity. Saturation intensity can be calculated as

$$I_s = \frac{h\upsilon_{ij}}{\sigma(\upsilon)\ \tau_R} \tag{11}$$

where h is Planck's constant, υ_{ij} is the frequency of the $i \rightarrow j$ transition, and τ_R is the total radiative lifetime of the transition, or the sum of all Einstein A coefficients associated with the upper state. Instead of just considering the radiative lifetime, the saturation intensity can also be calculated by including additional loss terms to the radiative lifetime. For this study, the temperature- and density-dependent spin-orbit mixing rate between p9 and p10, $k = 4.181\times10^6$ s^{-1} for a temperature of 400 K and total argon density of 1.2×10^{17} cm^3, was added to τ_R to calculate the saturation intensity. Assuming the pumping laser is at the center wavelength of the transition, as is normally done for this calculation, the saturation intensity was found to be 0.597 W/cm^2, 5.86 W/cm^2, 18.45 W/cm^2, and 31.05 W/cm^2 for pressures of 5 Torr, 100 Torr, 400 Torr, and 700 Torr, respectively. This resulted in theoretical bleaching intensities of 5.97 W/cm^2, 58.6 W/cm^2, 184.5 W/cm^2, and 310.5 W/cm^2. Using the definition of intensity, $I = P/A$, where P is power of the radiation and A is the area over which the radiation is incident, the maximum diameter that a pump beam of 900 mW could have been while still surpassing the bleaching threshold was 1,385.7 µm, 442.2 µm, 249.2 µm, and 192.1 µm.

A lens with a focal length of 100 mm, such as the one used for this research, should be able to focus a 1 mm beam spot to this size, but the beam divergence would also be large. The beam divergence of the Matisse TX beam after the focusing optic was calculated to be 5.9 mrad, too large for the focused beam to be measured by a Coherent ModeMaster which could measure a maximum divergence of 3.6 mrad. Because of this, the actual focused beam characteristics were not measured. Instead, the beam characteristics were measured just before the Faraday cage and propagated through the lens. The radius of the focused spot, w_F, was calculated using

$$w_F = \frac{\lambda f M^2}{\pi w_L} \tag{12}$$

where λ is the wavelength of the pump laser, f is the focal length of the lens, M^2 is the beam quality, and w_L is the spot radius before the focusing lens [15]. This gave a theoretical focused beam diameter, $2w_F$, of 88 μm. It was not believed that the focused beam diameter was actually this small, but the factor of two difference between the theoretical value and the smallest beam diameter required (192.1 μm) indicated the plasma would be bleached for all pressures. If the beam diameter was assumed to be 100 μm, bleaching would occur at pump powers over 0.47 mW, 4.6 mW, 14.5 mW, and 24.4 mW for pressures of 5 Torr, 100 Torr, 400 Torr, and 700 Torr, respectively.

The large divergence also brought into question the uniformity of the pumped discharge in the field of view of the fiber optic. It was possible that the total region of the discharge under observation was not bleached and a spatial dependence existed within the discharge. This certainly seemed to be case, as shown in Figure 10.

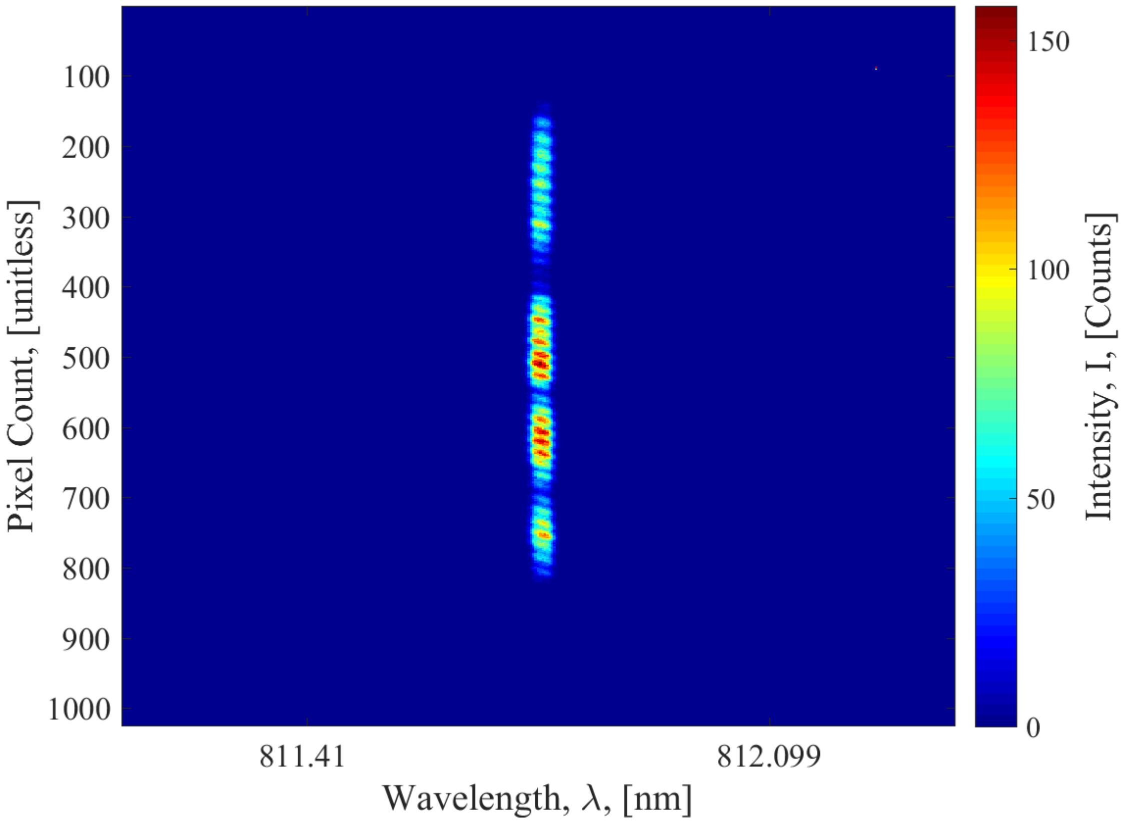

Figure 10. A false color, red-hot image of the output of the PI-MAX2 camera showing the relative throughput of the fiber cores in the fiber bundle. The red areas are where the intensity on the iCCD is the greatest. Each fiber core corresponds to 36 pixels measured vertically on the iCCD. This means each pixel represents roughly 8.3 μm on the face of the fiber optic.

There are two clear areas that have the greatest amount of intensity incident upon the iCCD, each about 36 pixels in vertical width. The approximate number of vertical pixels covered by a single fiber in the multi-fiber bundle was, in fact, 36. This means only two individual fibers had the focused spot in their fields of view. A visualization of this is shown in Figure 11. Because the area of interest is the bleached region of the discharge, only the rows on the iCCD corresponding to the two fibers viewing the focused spot were used in OES analysis. While doing this lessened the inaccuracy in the measurements due to the viewing volume, it was not believed to resolve the issue completely. For this reason, all numbers reported that involved measurements taken for the OES experiment were believed to be lower bounds.

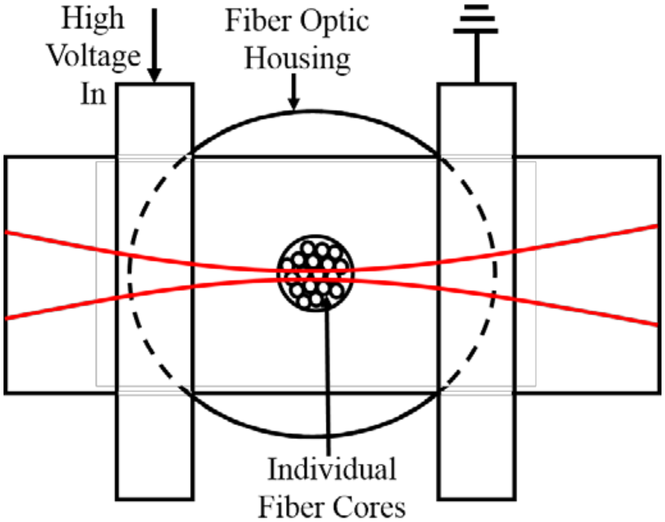

Figure 11. A visualization of the pump laser passing in front of the face of the fiber optic used during the OES experiment. Objects are not to scale as this figure was intended to increase understanding of the scenario introduced by Figure 10, not to portray the exact placement of the fiber optic or width of the pump laser as it passes through the test cell.

Once the viewing volume issue had been dealt with as best as possible, the data acquired to experimentally determine the bleaching intensity curve of the 811 nm transition was processed. The results are shown in Figure 12. Intensity curves such as this should increase linearly at low pump power before rolling off into a horizontal line as pump power increases past the bleaching limit. As can be seen in Figure 12, this was not observed. In the 5 Torr case a steep linear increase was seen before a slight roll off around 60 mW of pump laser power occurred, followed by a less steep linear increase. Both the 100 Torr and 400 Torr cases increased linearly for all pump laser powers with no evidence of a roll off. The 700 Torr case showed no clear behavior, which was most likely caused by the oscillating plasma passing into and out of the pump beam. For this reason, the 700 Torr case was ignored when evaluating pressure-related trends.

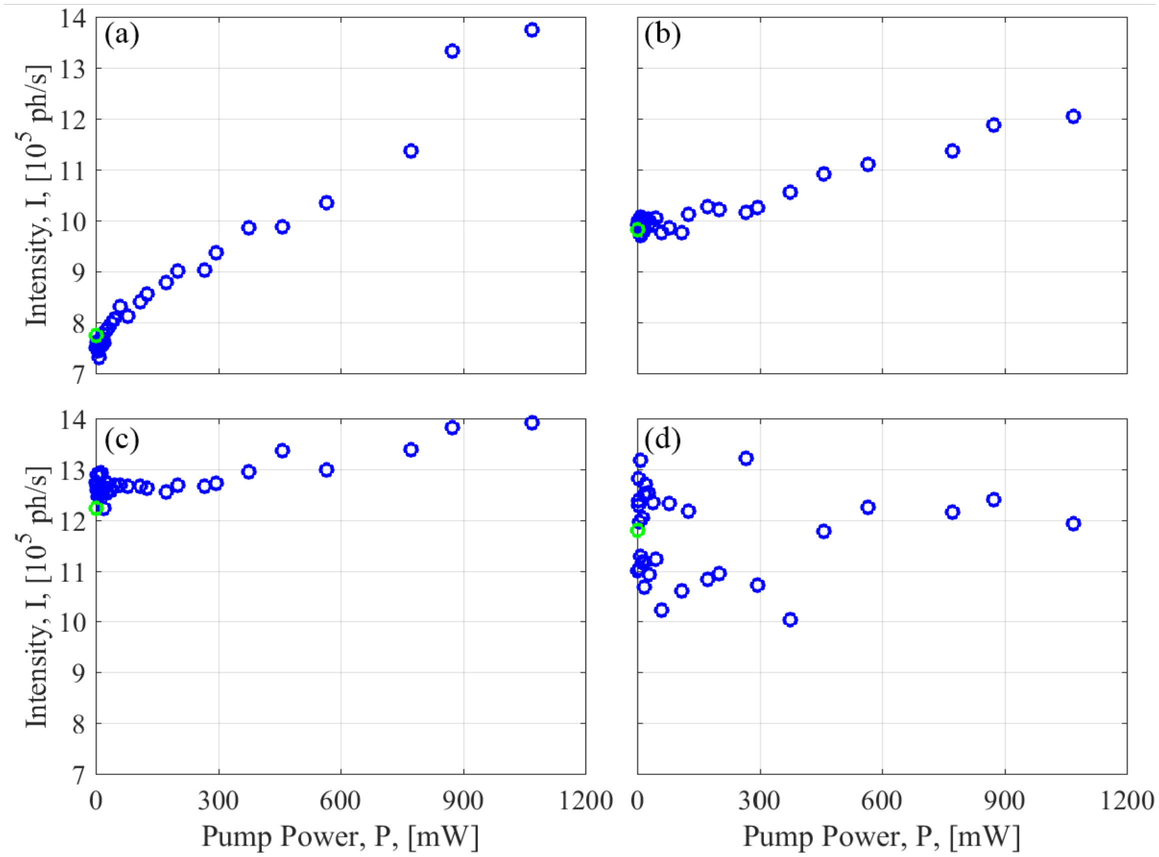

Figure 12. Plots (a), (b), (c), and (d) are the transition intensity curves for the 811 nm line for pressures of 5 Torr, 100 Torr, 400 Torr, and 700 Torr, respectively. The lone green data point in each plot was taken to check the reproducibility of the measurement when the pump beam was blocked.

The lack of a clear roll off into a horizontal line for all pressures could have been caused by two phenomena. The first would have been that the argon plasma was not being bleached for any power at any pressure. This was unlikely as the maximum calculated pump laser power required for bleaching was under 25 mW, and that was for the 700 Torr case. The second, and more likely, explanation was that the volume of the discharge being bleached increased as pump power increased. Because the pump laser beam was approximately a Gaussian wavefront, an increase in pump power increased the cross sectional area of the beam that was above the bleaching threshold, which increased the bleached volume in the discharge. If this was the case, as was assumed in this study, the constant increase in intensity indicated that the bleached limit was reached at low pump power for all pressures, which was consistent with the calculated values. The difference between the slopes of the intensity curves indicated that the nature of the plasma discharge changed as function of pressure, which was in agreement with Figure 5.

4.3 Optical Emission Spectroscopy

The amount of power in the pump beam was limited by the performance of the Matisse TX. On the particular day these data were taken, the pump beam was limited to about 850 mW. From the bleaching intensity calculations performed in Section 4.2 and the intensity curves shown in Figure 12, this was high enough to ensure the volume of the discharge under observation was bleached when subjected to the pump beam. A sample of the collected data was shown in Figure 10. The rows that contained the two fibers of interest, as discussed above, were summed column-wise to generate a spectrum. Sample spectra are shown in Figures 13, 14, and 15.

These spectra for the 801 nm (Figure 13), 811 nm (Figure 14), and 772 nm (Figure 15) transitions show all data taken for these transitions. The blue data points correspond to the unpumped data (just the fluorescence of the argon plasma discharge), and the red data points correspond to the pumped data. Each spectrum was purposely moved during post-processing to be centered on the line center wavelength for a pressure of 5 Torr. This was done because the reproducibility of monochromator motor placement during data acquisition was poor. This had no effect on data analysis. The spectra for all of the transition lines in Table 1 are given in Appendix C except for the 727 nm line. These plots show some of the data that went into the full spectrum sample in Figure 8. The 772 nm lineshape plot is shown specifically to help visualize where the data break was imposed.

From the spectrum in Figure 13, 14, and 15, a few key predictions about the discharge were confirmed. As pressure increased, the density of all p-states, except for p9, in the test cell increased (if the 700 Torr case was ignored). When the pump was applied, the density of p9 decreased as pressure increased, which indicated that spin-orbit mixing between the excited states did increase with pressure. The large decrease in both the pumped and unpumped densities was most likely caused by instability in the discharge at high pressure. At high pressure the main part of the discharge would oscillate spatially in the test cell, causing the discharge fluorescence to rapidly switch between being inside and outside the field of view of the fiber optic.

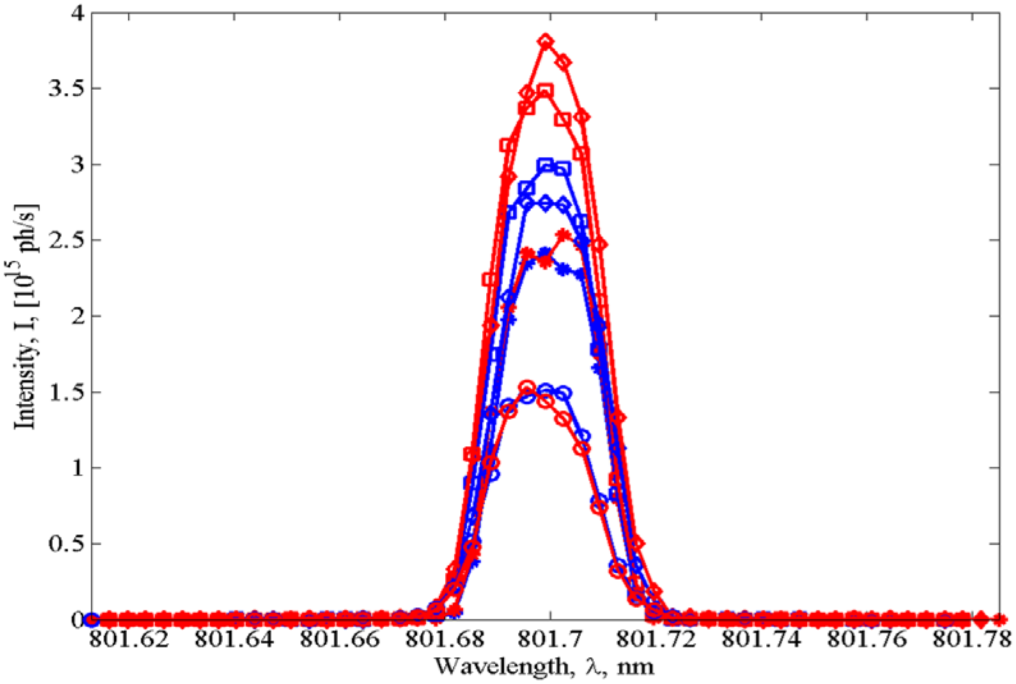

Figure 13. Sample spectra with all data taken for the 801 nm transition. The asterisks, squares, diamonds, and circles indicate the pressure in the test cell, 5 Torr, 100 Torr, 400 Torr, and 700 Torr, respectively. The blue data indicate unpumped data, while the red data indicate laser pumping. Error bars were omitted to reduce visual clutter. While data was only collected at the larger markers, lines are used to connect the markers to increase visual clarity.

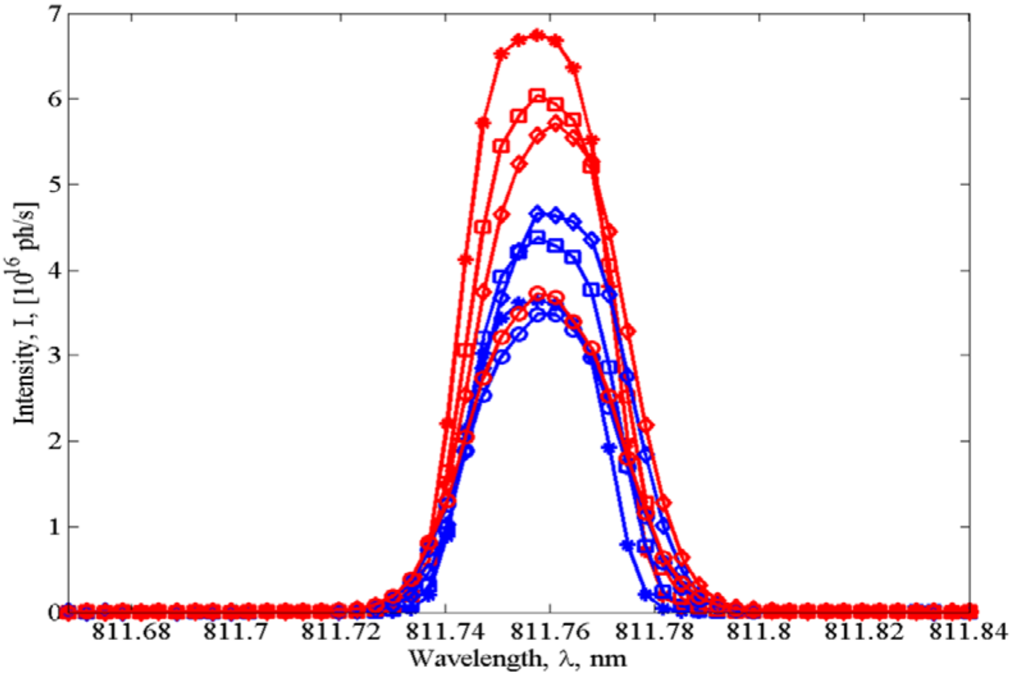

Figure 14. Sample spectra with all data taken for the 811 nm transition. All markers and colors follow the same convention as Figure 13.

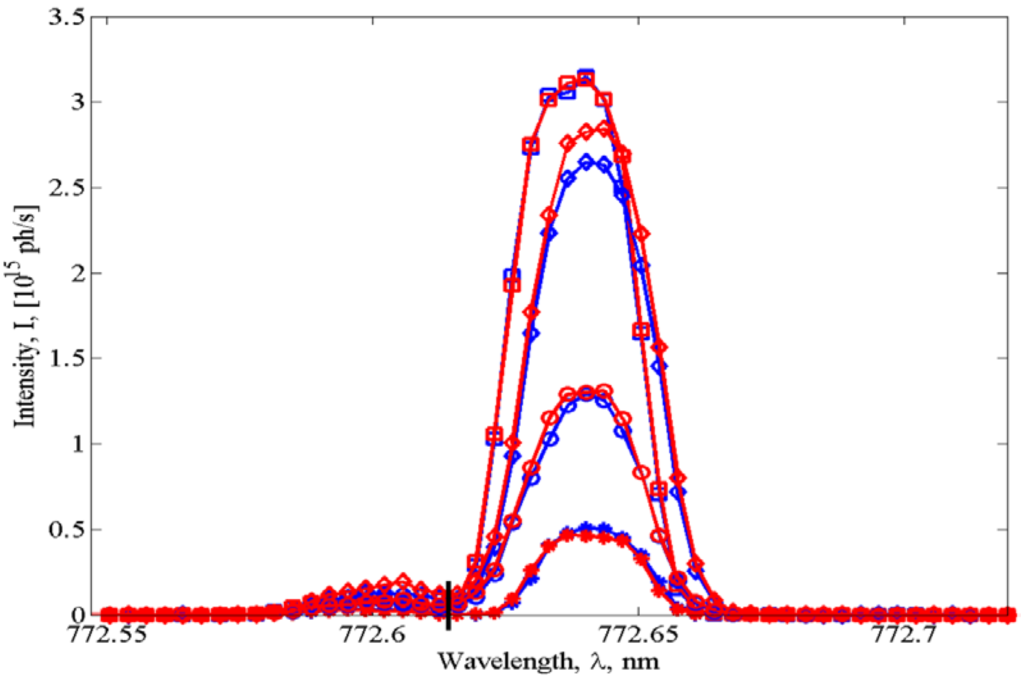

Figure 15. Sample spectra with all data taken for the 772 nm transitions All markers and colors follow the same convention as Figure 13. This spectra was included so the data break used to during analysis of the 772nm lines, represented by the thick vertical line, could be visualized.

By numerically integrating the acquired spectra, the relative densities of the p-states were found using Equation (2). The results of this process for all transitions are shown in Figures 16, 17, 18, and 19. The relative density in each p-state is shown as a function of p-state energy. The intensity on these plots is a slight misnomer. The densities were only found in a relative sense by using OES, so the values on the axis could have been anything as long as the interval spacing was held constant. All plots have the general trend that higher-energy p-states had lower densities, which was expected. For the 5 Torr case (Figure 16) all populations except for the p9 state stayed relatively constant, consistent with the belief that spin-orbit mixing was almost non-existent at this pressure. The p9 state relative density increased the most in the 5 Torr case relative to the other pressures. As pressured was increased, evidence of increased spin-orbit mixing was found. Many of the densities of the pumped discharge were noticeably higher than the unpumped densities for the 100 Torr case, and all of the pumped densities were noticeably higher for the 400 Torr case. For almost all p-states, the densities for both the pumped and unpumped conditions were higher in the 100 Torr case than in the 400 Torr case, which was almost always higher than the 700 Torr case. The densities for the 5 Torr case were not consistently higher or lower than any other pressure.

The error bars in Figures 16, 17, 18, and 19 were generated by adding the uncertainties of the acquired intensity data and the Einstein A coefficients, or

$$Error = \sqrt{\left(\frac{dI}{I}\right)^2 + \left(\frac{dA_{ij}}{A_{ij}}\right)^2} \tag{13}$$

where dI was the statistical uncertainty in the intensity and dA_{ij} was the uncertainty in the Einstein A coefficients. The statistical uncertainty in the data was taken as the standard deviation of the acquired spectra, and the Einstein A coefficients have a 50% uncertainty. Because the standard deviation of the acquired spectra is small, the error was almost always dominated by the Einstein A coefficient uncertainty. Therefore, the error almost always had a value of 0.5. Only the 706 nm line was consistently affected by the uncertainty in the intensity, but that effect was two orders of magnitude smaller than the Einstein A coefficient uncertainty.

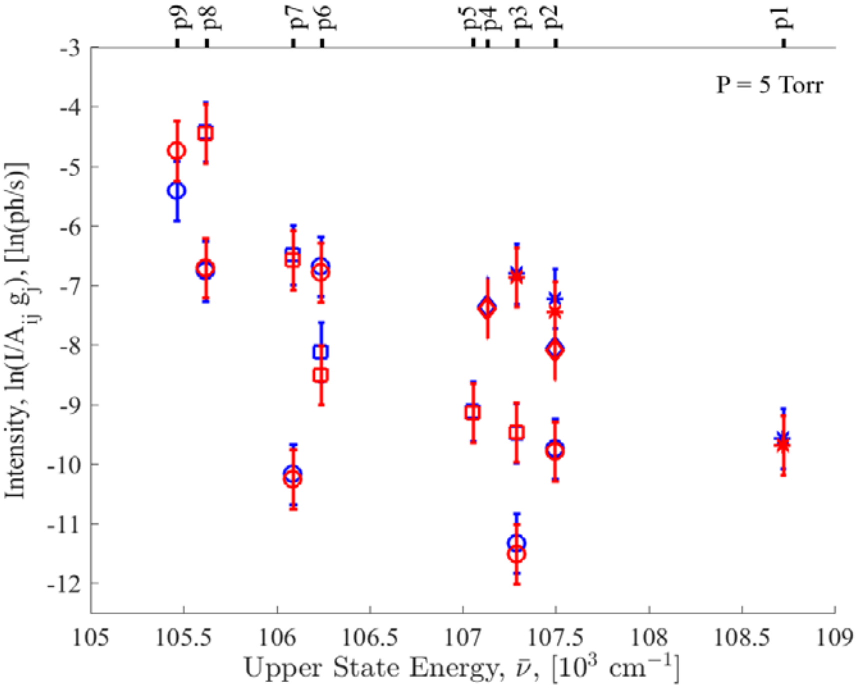

Figure 16. The relative population versus p-state energy for all of the transitions listed in Table 1 for a pressure of 5 Torr. The circles represent transitions with the lower state of s5, squares for s4, diamonds for s3, and asterisks for s2. The blue colored markers indicate unpumped acquisitions, while the red colored markers indicate pumped acquisitions.

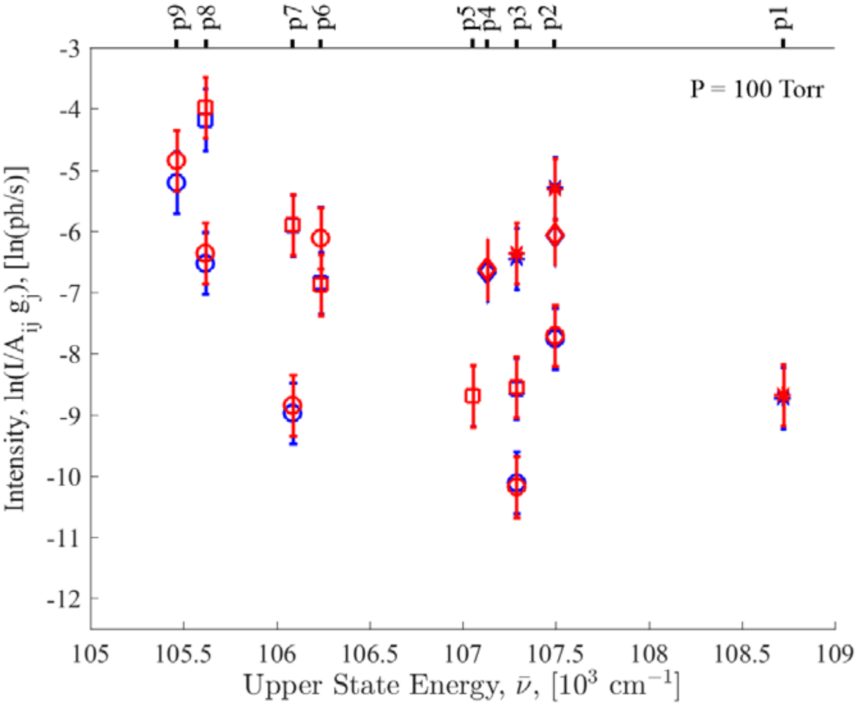

Figure 17. The relative population versus p-state energy for all of the transitions listed in Table 1 for a pressure of 100 Torr. All markers and colors follow the convention established in Figure 16.

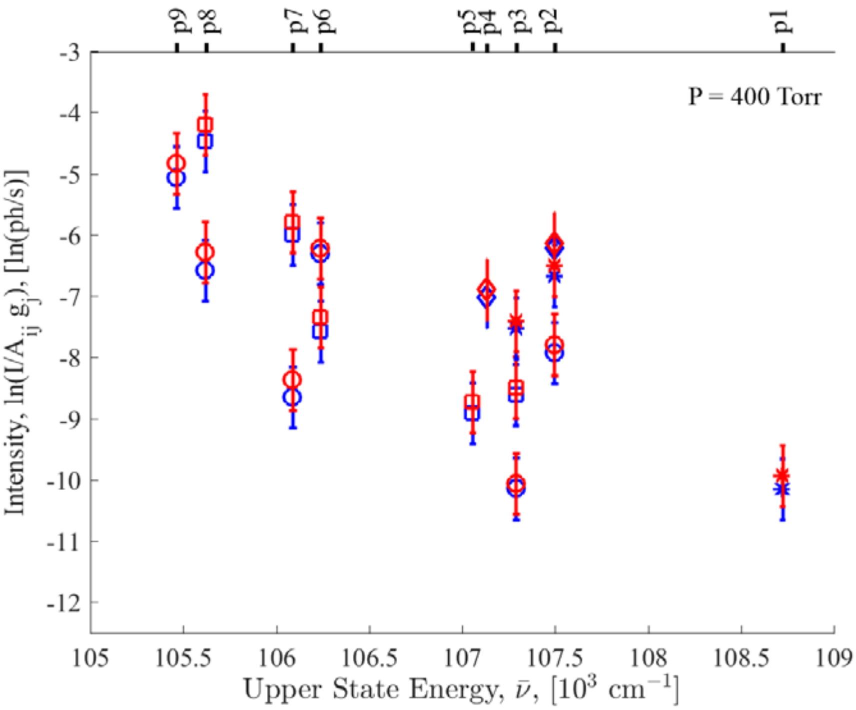

Figure 18. The relative population versus p-state energy for all of the transitions listed in Table 1 for a pressure of 400 Torr. All markers and colors follow the convention established in Figure 16.

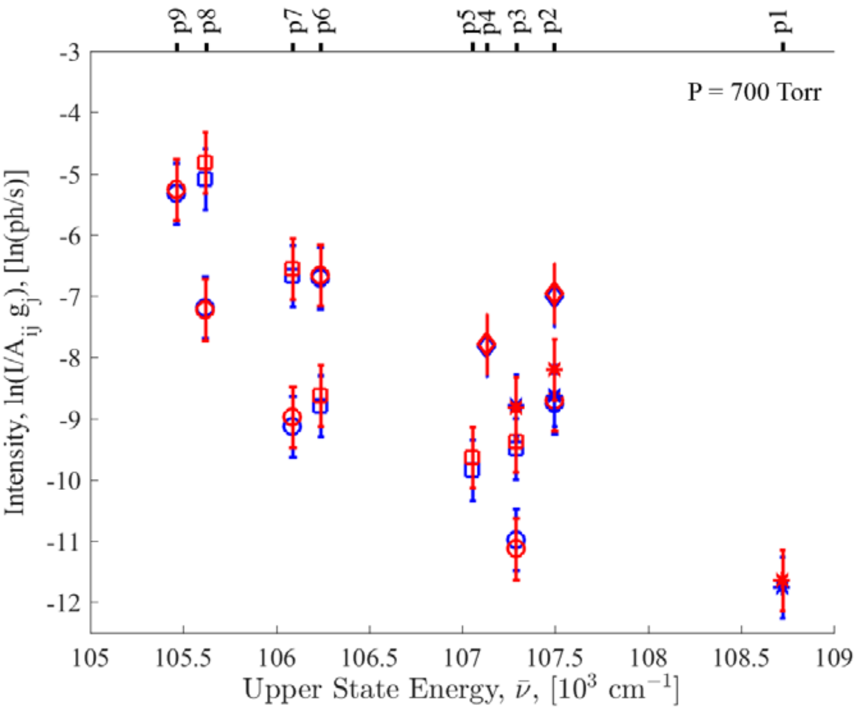

Figure 19. The relative population versus p-state energy for all of the transitions listed in Table 1 for a pressure of 700 Torr. All markers and colors follow the convention established in Figure 16.

In Figures 16-19, a curious feature caused concern. If a p-state is involved in more than one transition, all of the data points for that state at the same pressure and pumping condition should have been overlapping. If the points were not overlapping, multiple different values for the relative density of the p-state were reported which is not physically possible. As can be seen, the same-case data points for the p-state relative densities did not overlap even when the total uncertainty in the measurements were taken into account. This indicated that some factor was being left out of the relative density calculation. It was found that the lower the reported values for relative densities were, the weaker the emission of the transition line. While this may be a topic for future research, it is not the focus of this research and will not be discussed further.

As previously mentioned, the differences, not the reported magnitudes, of the relative populations was the desired piece of information. These are shown in Figures 20, 21, 22, and 23. For every transition collected, with the exception of the 811 nm line, the difference between the relative population in the pumped and unpumped conditions increased with an increase in pressure (again, ignoring the 700 Torr case), as indicated by the differences becoming more positive. For the 811 nm transition, the difference in relative population decreased with an increase in pressure. These two effects were anticipated and showed that spin-orbit mixing had a greater effect at higher pressures. The negative values found for many of the transitions were believed to be caused by the pump laser changing the nature of the discharge. For the 5 Torr case, all transitions except the 811 nm line had almost no change in population. As pressure was increased to 100 Torr, the p-states closest to the pump transition began to rise, as expected. The closer in energy the p-states were, the smaller the potential barrier between the states was.

Raising the pressure to 400 Torr further increased the population density of the energetically closer p-states when the discharge was pumped, but also increased the population density of the p-states higher in the manifold enough so that all pumped-unpumped population density differences were positive. As was expected, no clear trend in the 700 Torr data was found because of the instability of the plasma at this pressure. Error for this data was taken to be just the statistical variation in the acquired transition line intensities because any uncertainty in the Einstein A coefficient would be present in the pumped and unpumped data equally. By combining this information with the absolute density information found during the TDLAS experiment discussed below, the upper bound of the absolute population density moved into each state was found.

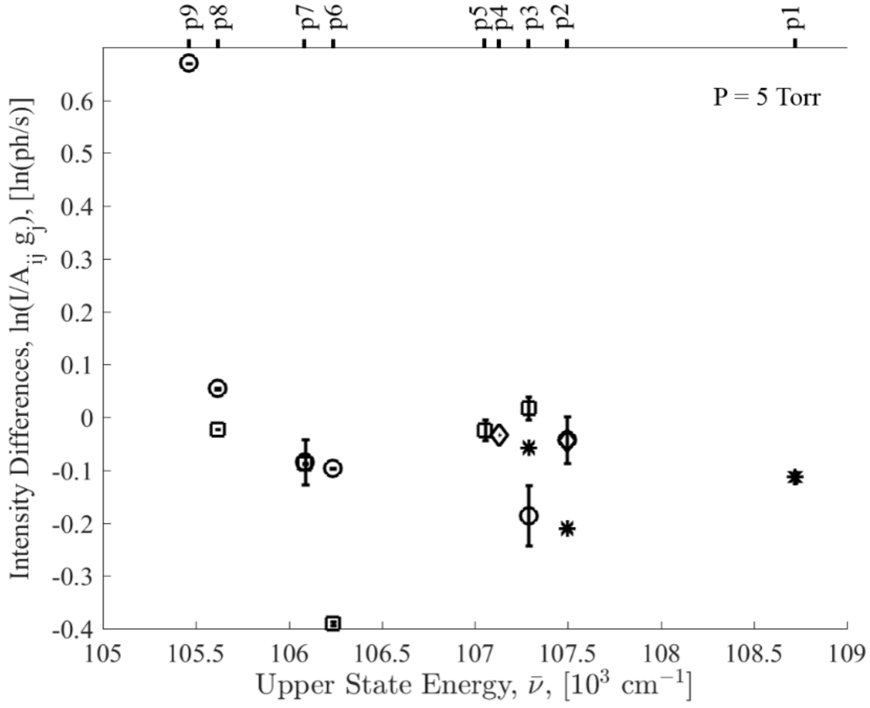

Figure 20. The differences between the relative population densities of the p-states when subjected to pumping plotted against p-state energy for a pressure of 5 Torr. The shape of the data point denotes the lower state of the transition: circle for s5, square for s4, diamond for s3, and asterisk for s2. Positive differences indicate population growth due to pumping, while negative differences indicate population loss.

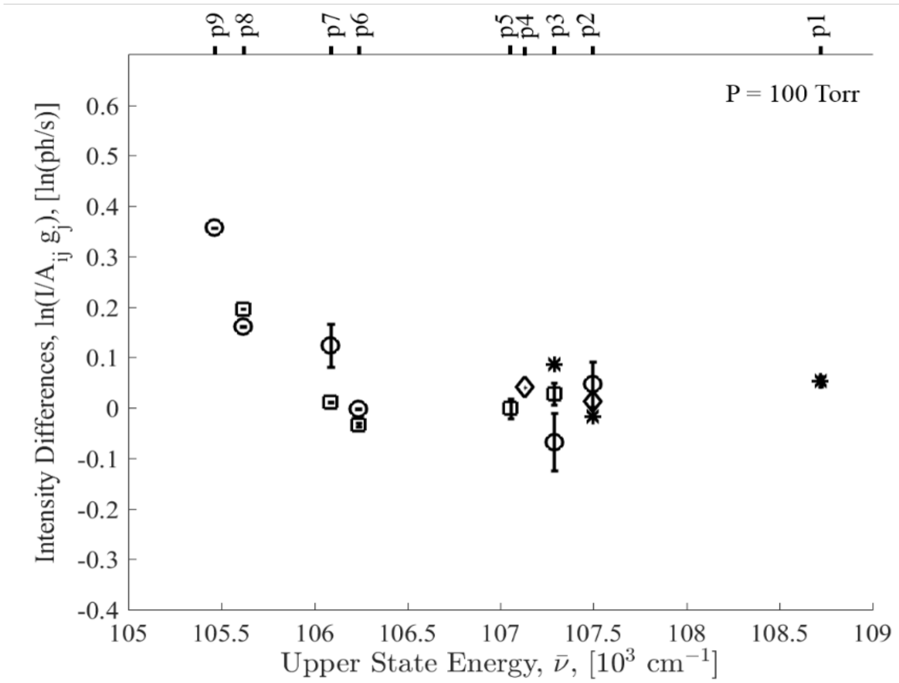

Figure 21. The differences between the relative population densities of the p-states when subjected to pumping plotted against p-state energy for a pressure of 100 Torr. All markers follow the same convention as Figure 20.

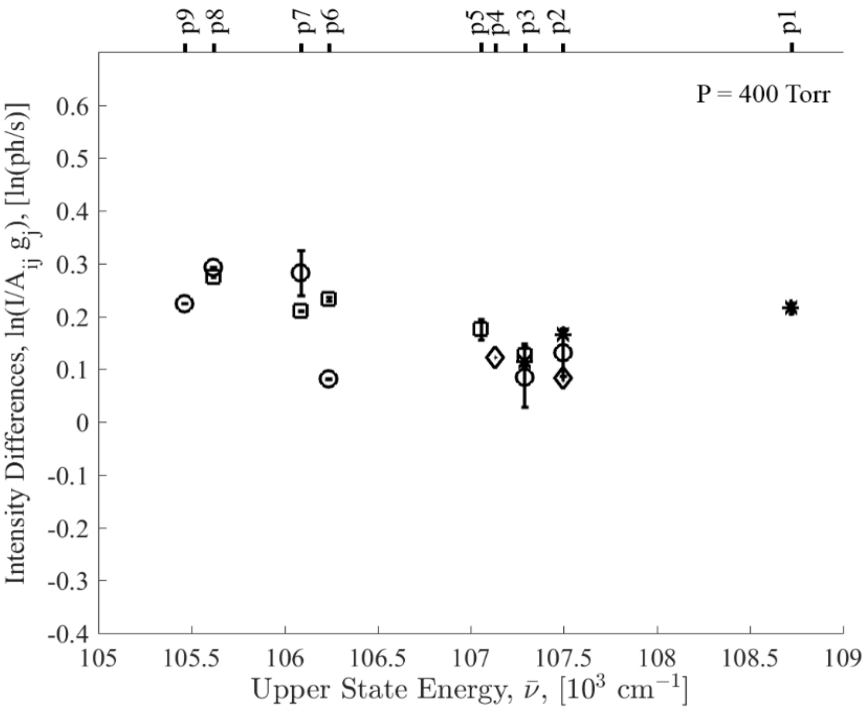

Figure 22. The differences between the relative population densities of the p-states when subjected to pumping plotted against p-state energy for a pressure of 400 Torr. All markers follow the same convention as Figure 20.

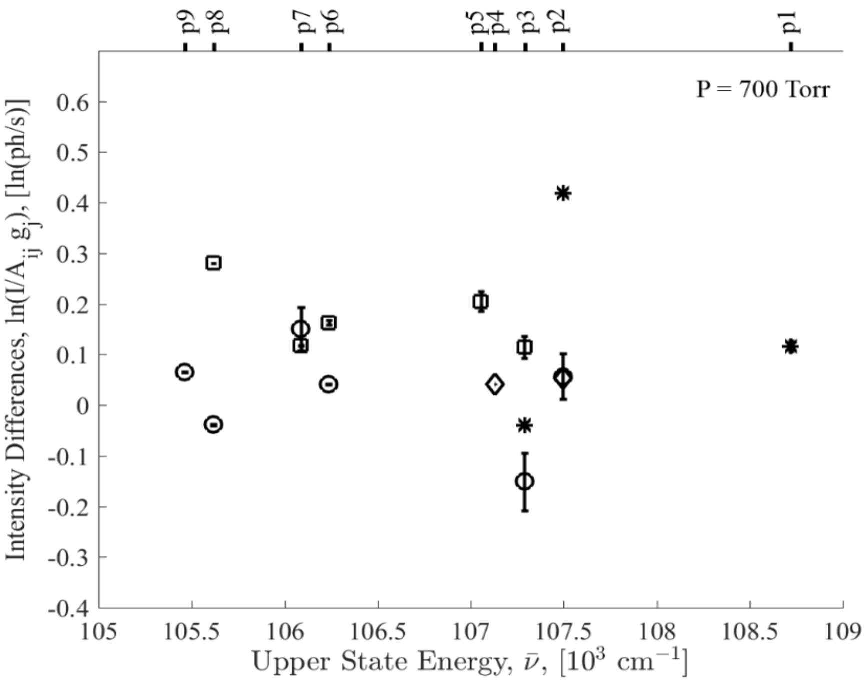

Figure 23. The differences between the relative population densities of the p-states when subjected to pumping plotted against p-state energy for a pressure of 700 Torr. All markers follow the same convention as Figure 20.

4.4 Tunable Diode Laser Absorption Spectroscopy

The absorption curves acquired for the 5 Torr case are shown in Figure 24. As was expected, the absorption curves, as a function of relative probe laser frequency, decreased in magnitude as the pump power increased from 10 mW (light green) to 899 mW (dark green). A relative frequency axis was used because the actual frequency did not matter, just that the probe laser wavelength was scanning through the appropriate transition. Every pumped curve had the tell-tale Bennet hole with a Doppler-broadened lineshape, confirming the 5Torr case was not dominated by collisions and that the pump power was higher than the bleaching intensity for pump powers as low as 10 mW. The top of the unpumped absorption profile appeared noisy because the discharge was near opacity, or complete optical thickness to the wavelength, when the probe laser scanned near the center wavelength of its associated transition (p8→s5).

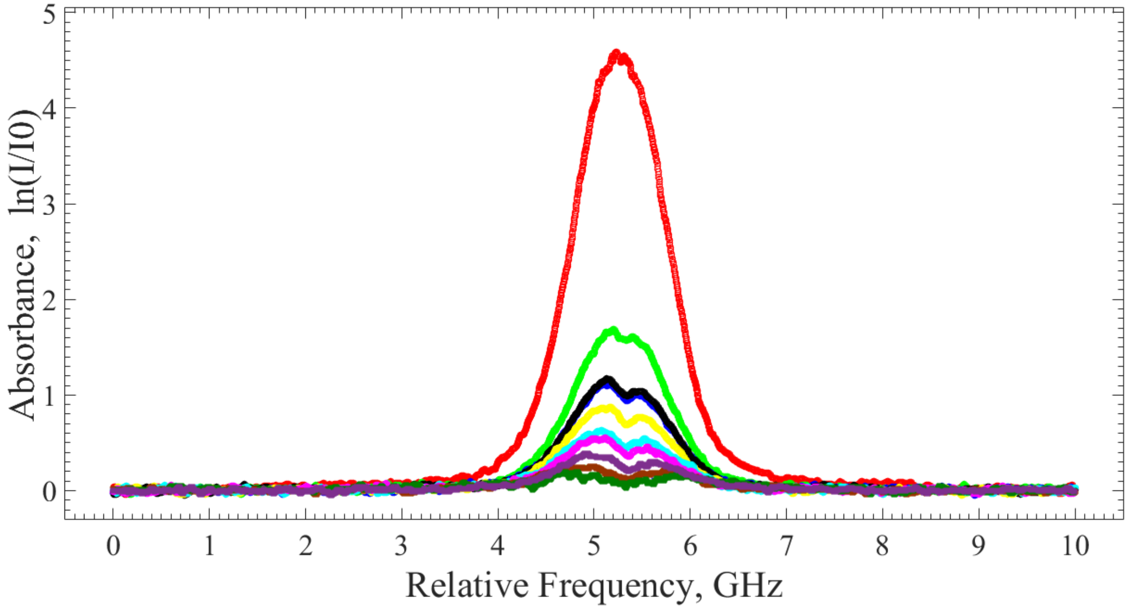

Figure 24. The absorption curves as a function of relative probe laser frequency for the data acquired when pressure inside the test cell was 5Torr. The red line is the absorption profile with only the scanning probe beam passing through the discharge (no pump beam). The various colors are the absorption profiles for different pump beam powers, light green for 10 mW, dark blue for 16 mW, black for 19 mW, yellow for 34 mW, cyan for 66 mW, magenta for 146 mW, purple for 231 mW, brown for 488 mW, and dark green for 899 mW.

The first step after acquiring the absorption curves was to fit the data. The unpumped absorption curve, indicated by the red line in Figure 24, was fit with a Voigt profile and the resulting integrated absorption underwent the analysis presented in Section 2.2. All pumped curves were fitted with the Lamb dip absorption profile presented in Section 2.3. All fits were performed using a MATLAB® script developed by Dr. Christopher Rice, Dr. Kevin Gross, and Mr. Ben Eshel at the Air Force Institute of Technology. The resulting fits and residuals are shown in Figure 25. The magnitude of the residuals of all fitted pumped curves was never greater than 0.075. Residuals for the

Voigt fit of the unpumped curve were not included because the opacity of the discharge restricted the peak absorbance recorded and resulted in errors greater than 0.2, which washed out the other residuals. The lack of structure in the residuals indicated the Lamb dip absorption profile could have been the appropriate fit function.

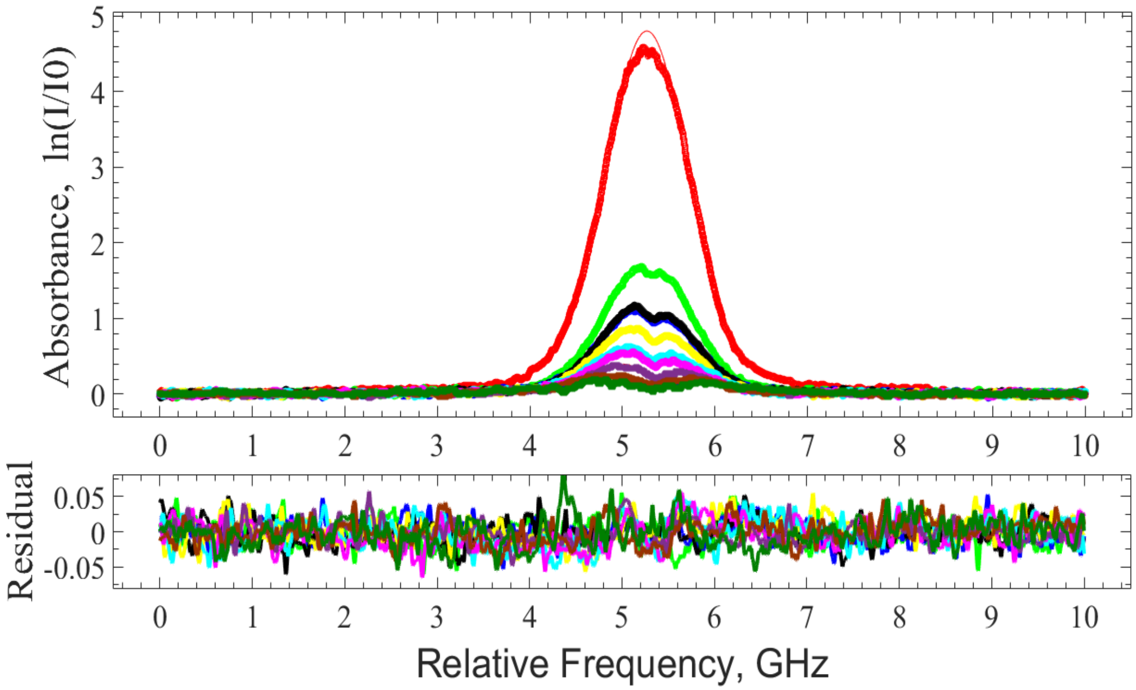

Figure 25. The absorption curves, absorption curve fits, and the fit residuals for a test cell pressure of 5 Torr. The color scheme corresponds to that of Figure 24.

From the Voigt fit of the unpumped curve, the population density in the s5 state when the discharge was not subjected to any pump laser was found to be 7.4×10^{11} cm^{-3}. As the pump power increased, the absorption curve approached the zero absorption, or transparency, limit. In the transparency limit, it can be assumed that the population density moved into the p9 state is equal to the unpumped population density in the s5 state multiplied by branching ratio of the energy states, or

$$\Delta n_{p9} = \frac{g_{p9}}{g_{s5} + g_{p9}} n_{s5}^{0} \tag{14}$$

where g_i is the degeneracy of the specified state, calculated as $2J + 1$, and n_{s5}^{0} is the unpumped population density in the s5 state. This meant that the population density moved into the p9 state when the argon discharge was bleached was 4.3×10^{11} cm^{-3}. From Figure 12 it was found that the population density in the p9 state about doubled between the unpumped and the 875 mW pump laser power cases, meaning the population in the p9 state was about 4.3×10^{11} cm^{-3} before the discharge was optically pumped. The amount of population moved from the s5 state to the p9 state as a function of pump laser power was also found, and is shown in Figure 26.

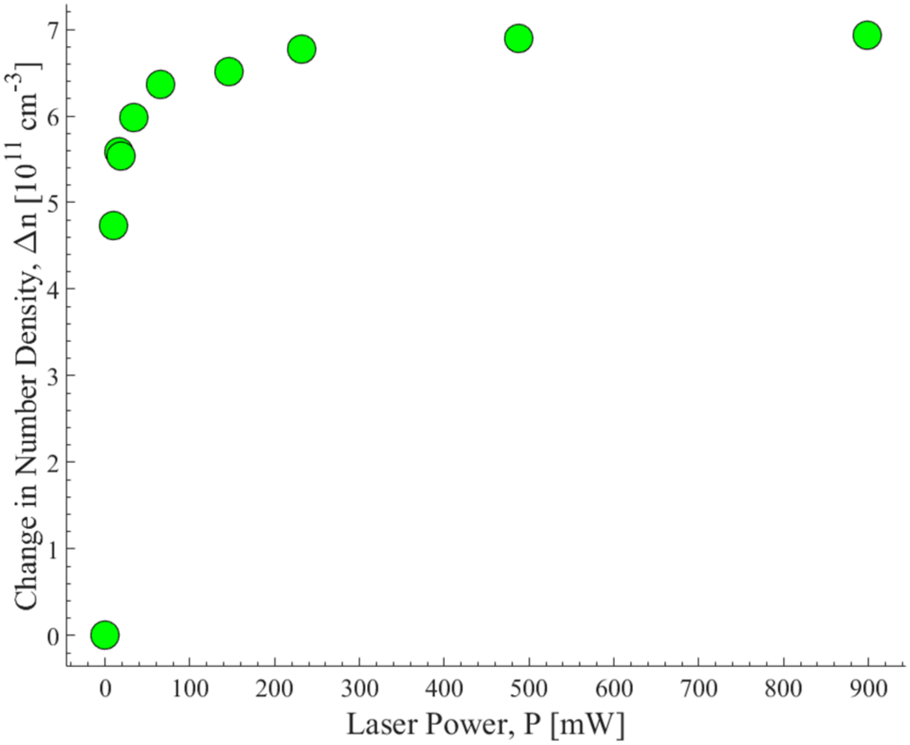

Figure 26. The population density moved from the s5 to the p9 state as a function of pump laser power. As pump power increased, the population density moved increased rapidly before rolling off. This indicated bleaching of the discharge occurred around 250 mW.

From this figure it appeared that bleaching of the discharge did not occur until the pump laser power was about 250 mW, which was almost three orders of magnitude greater than the calculated value. Another issue with this figure is the moved population density was calculated by allowing the ΔN_0 in Equation (8), which is a constant, to change when fitting the absorption curves. Both of these problems were most likely caused by a propagation length dependent pump beam intensity that was not accounted for in the fit function. The assumption of a constant intensity beam used in the Lamb dip equation was not valid because of the high beam divergence referenced in Section 4.2. Adjusting the intensity to have a propagation distance dependence may resolve both of these issues.

If the values in Figure 26 are taken to be correct despite the problems presented, the maximum population change of 6.9×10^{11} cm^{-3} can be equated to the difference between the unpumped data point and the pump power of 875 mW data point from Figure 12 (a) to create a population density calibration factor of 1.19×10^{6} cm^{-3}/(ph/s). This population density factor was multiplied to all data points in Figure 12, including those at pressures other than 5 Torr, to find the absolute population density moved into the p9 state as a function of pump laser power. The multiplication factor was used for all pressures because it was a pressure independent factor. The results of the multiplication are shown in Figure 27. As can be seen from Figure 27 (a), the experimentally found population density at a pressure of 5 Torr is almost a factor of two greater at all points than was expected. This difference was believed to be caused by not accounting for either the radial dependence of the bleached volume due to pump power or the propagation distance dependence of the pump laser intensity inside the test cell.

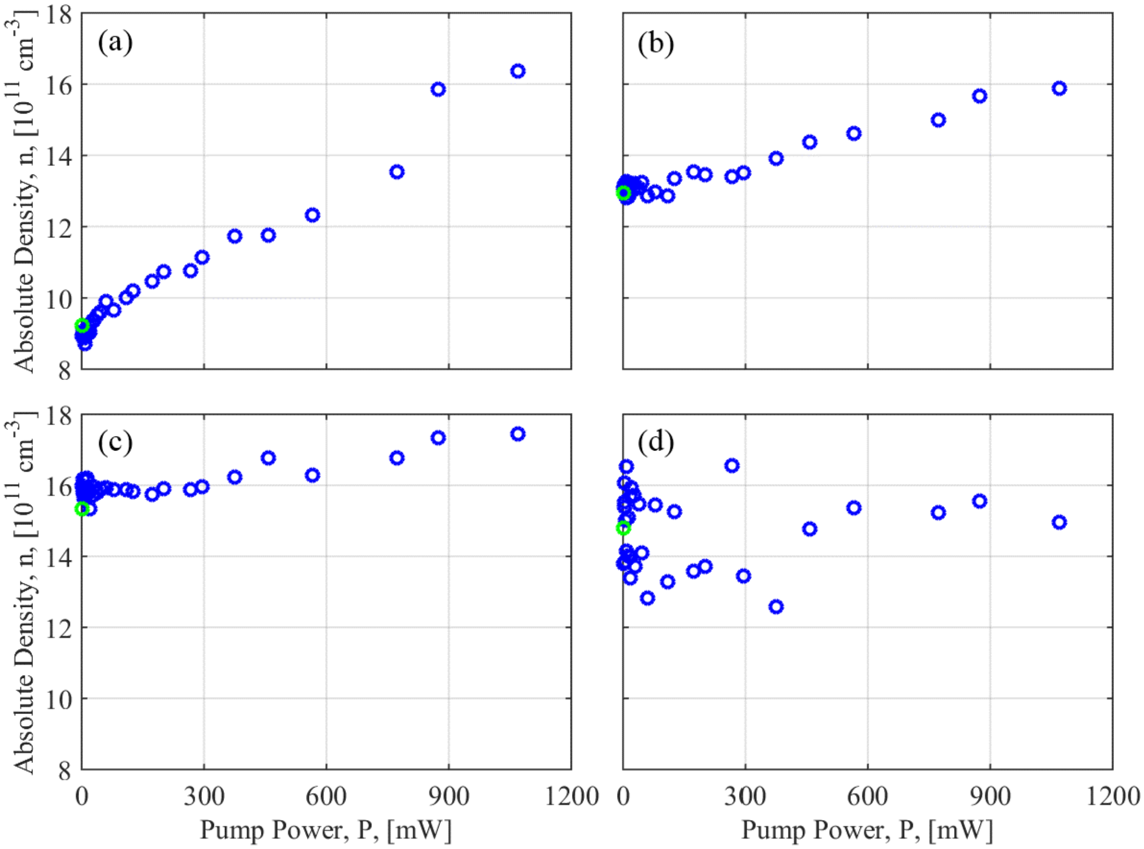

Figure 27. Absolute population density in the p9 state for the 811 nm line as a function of pump laser power for test cell pressure of (a) 5 Torr, (b) 100 Torr, (c) 400 Torr, and (d) 400 Torr.

The population densities moved into the other p-states were found in a similar manner. Instead of using the maximum population change of 6.9×10^{11} cm^{-3} with Figure 12 (a), it was equated to the p9 data point in Figure 20 to create a population density calibration factor of 1.03×10^{12} cm^{-3}/ln(ph/s). Multiplying this factor to every difference in Figures 20-23 resulted in the population density moved into the excited state for each transition and pressure recorded. These results are shown in Table 2. The uncertainties listed in the table were calculated using only the statistical variation in the acquired transition line intensities, as was done for Figures 20-23.

Table 2. Population Movement between P-States

			P = 5 Torr		**P = 100 Torr**		**P = 400 Torr**		**P = 700 Torr**	
Vacuum Wavelength (nm)	**Upper State**	**Lower State**	**Δn 10^{11} cm^{-3}**	**±Δn 10^{8} cm^{-3}**	**Δn 10^{11} cm^{-3}**	**±Δn 10^{8} cm^{-3}**	**Δn 10^{11} cm^{-3}**	**±Δn 10^{8} cm^{-3}**	**Δn 10^{11} cm^{-3}**	**±Δn 10^{8} cm^{-3}**
750.5935	p1	s2	-1.17	7.77	0.55	6.65	2.24	13.79	1.21	16.43
696.7352	p2	s5	-0.44	32.67	0.49	7.99	1.36	13.97	0.59	16.48
727.494	p2	s4	1.85	223.85	2.36	46.04	3.82	56.59	2.14	100.60
772.6333	p2	s3	-0.46	3.64	0.14	0.74	0.86	1.33	0.56	2.38
826.6794	p2	s2	-2.18	0.60	-0.18	0.24	1.72	0.25	4.33	1.32
706.9167	p3	s5	-1.92	41.67	-0.70	34.19	0.88	29.19	-1.56	70.19
738.6014	p3	s4	0.18	18.98	0.28	8.58	1.31	5.61	1.19	10.05
841.0521	p3	s2	-0.59	0.09	0.89	0.17	1.19	0.10	-0.41	0.12
795.0362	p4	s3	-0.35	1.24	0.43	0.62	1.27	1.35	0.43	2.53
751.6721	p5	s4	-0.25	13.94	-0.01	5.93	1.82	2.68	2.12	1.95
763.7208	p6	s5	-1.00	0.45	-0.02	0.43	0.84	1.02	0.43	1.37
800.8359	p6	s4	-4.03	2.99	-0.34	1.54	2.41	1.32	1.69	3.38
772.5887	p7	s5	-0.88	3.64	1.28	0.74	2.93	1.33	1.56	2.38
810.5921	p7	s4	-0.90	0.43	0.12	0.24	2.18	0.54	1.22	0.50
801.699	p8	s5	0.56	0.93	1.67	0.61	3.03	0.46	-0.40	1.18
842.6963	p8	s4	-0.23	0.06	2.03	0.03	2.84	0.05	2.90	0.07
811.7542	p9	s5	6.94	0.08	3.69	0.07	2.32	0.10	0.68	0.32

With these results, some of the previously made conclusions regarding population density were verified. As pressure increased to 400 Torr the population density in all observed p-states, except for the p9 state, increased by about a factor of 4, which indicated spin-orbit mixing increased as a function of pressure. The population density moving from different lower states into the same excited state were not equal which indicated there were unknown processes taking place in the plasma discharge. It is also to be remembered that the population density changes reported were upper bounds. From this table, it was also seen that the population density moved into p2 rose more quickly than all other states except for p8. The movement into p8 was expected because the p8 energy level is only about 150 cm^{-1} higher than p9, but the p2 state is over 2000 cm^{-1} higher than p9. Some form of energy transfer, such as a large collisional cross section between states, exists. While the difference in the population density moved into the same excited state was troubling, the amount of population density moved increased at the same rate for all transition lines with the same upper state except for p6. Both lines with this upper state, the 763 nm and 800 nm lines, increased rapidly, but the difference in population density moved between the 5 Torr and 400 Torr cases was four times greater for the 800 nm line. This suggested a deeper effect than statistical variation was present. The magnitudes of the changes in population density suggested the population density in s-states and the p-states were about the same when the discharge was optically excited.

To correct for the radial dependence of the bleached volume, the area of the pump laser greater than the bleaching intensity, A_b, was found using

$$A_b = \frac{\omega_0^{\,2}\pi}{2}\ln\left(\frac{I}{I_b}\right) \tag{15}$$

where ω_0^2 is the beam waist and I_b is the bleaching intensity, which was estimated to be some multiple of the saturation intensity. The bleached area was only found at the beam waist in order to decouple the radial dependence and the propagation distance dependence. Two different values for the bleaching intensity, the saturation intensity and ten times the saturation intensity, and two different methods to find those bleaching intensities, by mathematical calculation and from the saturation parameter found during the TDLAS experiment, were used to find lower and upper bounds of the effect of this correction. The corresponding bleached areas at the beam waist as a function of pump power are show in Figure 28. The calculated bleached areas were always greater than those found experimentally, and, as expected, the bleached areas based on the saturation intensity were greater than those based on ten times the saturation intensity. The mathematically calculated bleaching intensities and the experimentally found bleaching intensity equal to the saturation intensity had non-zero values for bleached areas for pump laser powers greater than 30 mW. The experimentally found bleaching intensity equal to ten times the saturation intensity had non-zero values for bleaching areas for pump powers greater than 300 mW.

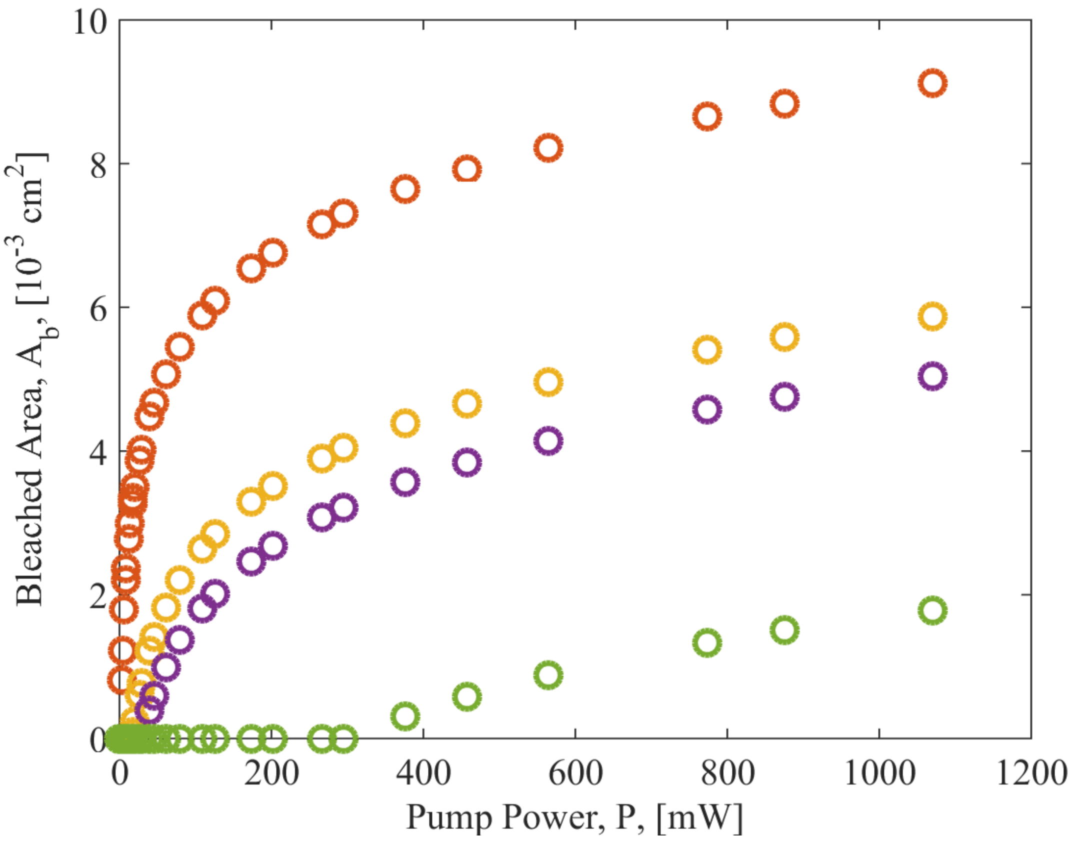

Figure 28. Bleached areas at the beam waist as a function of pump power. Both the mathematically calculated value for bleaching intensity and the bleaching intensity value calculated from the TDLAS experiment were used. The data points show the bleached area if the bleaching intensity was taken as the calculated saturation intensity (red), ten times the calculated saturation intensity (yellow), the experimentally determined saturation intensity (purple), and ten times the experimentally determined saturation intensity (green).

For each bleaching intensity, ratios of bleached area for a given pump laser power to the bleached area at the lowest pump laser power with a non-zero bleached area were then multiplied by the population density at the given pump power. The result of this multiplication for the 5 Torr case is shown in Figure 29. It was obvious that the bleaching intensity used to calculate the bleached area had a significant effect on the population density reported. The true bleaching intensity of the plasma discharge was also determined to be lower than both experimentally determined bleaching intensities because signal was seen after the test cell for pump laser powers greater than 10 mW, as seen in Figure 24.

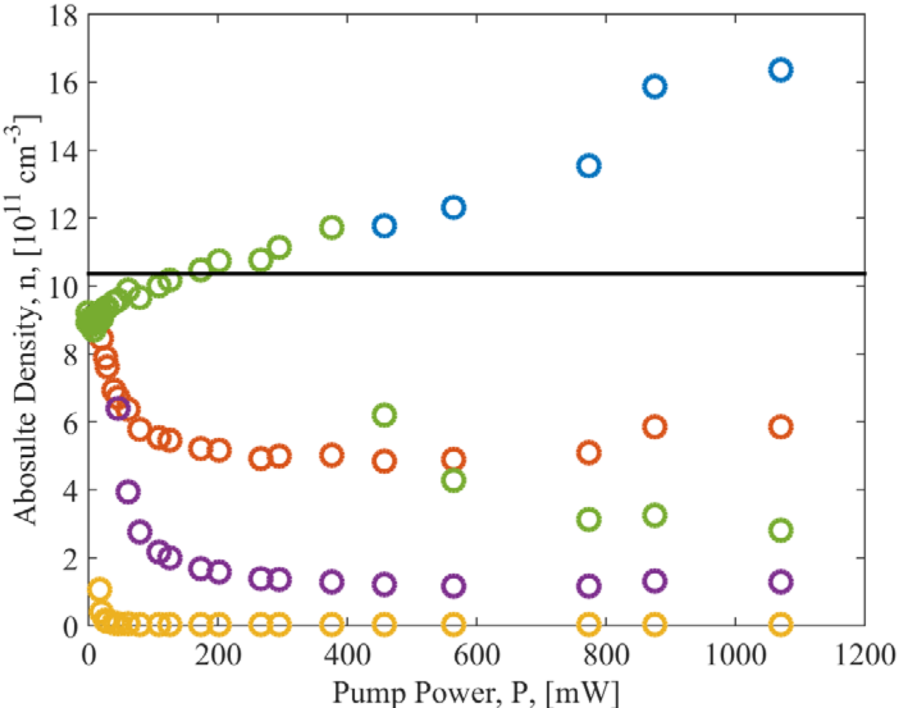

Figure 29. Bleached area-corrected absolute density in the p9 state as a function of pump laser power for a test cell pressure of 5 Torr. The blue data points are the measurements from the OES experiment, and the other colors correspond to the bleaching intensity used, red for the mathematically calculated saturation intensity, yellow for ten times the mathematically calculated saturation intensity, purple for the experimentally determined saturation intensity, and green for ten times the experimentally determined saturation intensity. The blue and green data points overlap for pump laser powers between 0 mW and 400 mW. The black line represents the gain threshold.

The gain threshold line, calculated as 10.36×10^{11} cm^{-3} by multiplying the unpumped s5 population density with the ratio of the degeneracies of the p9 state to the s5 state, is also shown in Figure 29. The uncorrected intensity curve suggested gain in the system, which was not seen in the absorption curves gathered during the TDLAS experiment. Because the bleached area correction pulled the population density in the p9 state below the gain threshold for all but one bleaching intensity used in Figure 29, the radial dependence on the bleached area within the discharge may have been a significant factor ignored when calculating the p9 population density. But, because all of the corrected data in Figure 29 were eventually inverted from what was expected, this may have not been the dominant source of error. To find the full correction factor, the bleached volume as a function of radial distance away from beam center and propagation distance must be found. To do this, Figure 26 must be corrected so that all data points fall on a line at Δn equals zero. This is a non-trivial correction, and, due to time constraints, was not performed.

V. Conclusions and Recommendations

5.1 Conclusions

By using optical excitation and tunable diode laser absorption spectroscopy, the effects of optical excitation of the argon s5→p9 transition and pressure on the population densities of the p-states in an argon discharge were examined. The population difference in the p9 state between the pumped and unpumped conditions decreased and the population differences in all other p-states increased as a function of pressure. This indicated significant redistribution of population into other p-states due to spin-orbit mixing. The increase in population density moved decreased as a function of upper state energy from p8 to p3. The large increase in the p8 state was expected due to the closeness in energy level to p9, but it was unexpected that the p2 state experienced the second largest increase in population density. A Bennet hole was observed and characterized for all lineshapes, which indicated a high degree of saturation at modest pump powers. Through the combination of OES and TDLAS, the population in the s5 state at 5 Torr before optical pumping was about 7×10^{11} cm^{-3}. This pointed to a population density of 4×10^{11} cm^{-3} in the p9 state before optical pumping. For the 5 Torr pressure case, this population increased by about a factor of two.

5.2 Significance

This study showed that increasing the pressure would increase the population density of all p-states at higher energies than p9, but would adversely affect the inversion of the s5→p9 transition. This redistribution of energy to other p-states is promising as the RGL requires significant amount of population to be moved from the p9 state into the p10 state. The Bennet hole indicated the degree of saturation was high, meaning the high power laser requirement of bleaching the gain medium is possible even at modest pump powers. Unfortunately the argon discharge system used does not appear to be in the gain region, which indicates a higher population density in s5 is needed for RGL development. This will require the design of an argon plasma discharge tailored to generate a greater excited argon population at high pressure. The data acquired during this thesis can also be used to augment or validate argon plasma discharge simulations, such as the ZDPlasKin model being developed at the Air Force Institute of Technology.

5.3 Recommendations for Future Research

If this topic is researched in the future, it is recommended that a different discharge is used due to the plasma striations present at low pressure and plasma column oscillations at high pressure. If a different discharge is produced that is stable at atmospheric pressure, it should be subjected to a similar study but focused on pressures above 500Torr. If a different discharge is not used, the plasma discharge behavior should be characterized and better understood so that the results found are more accurate. A switch should also be made from a multi-core, multi-mode fiber to a single-core fiber to solve some of the viewing volume issues. Any future research should also include an analysis of the p10 state due to its importance to the rare gas laser. It may also be useful to observe the population changes when the pump laser is not above the bleaching threshold. This information would not be directly useful to the rare gas laser, but it could deepen the understanding of the background argon plasma kinetics. A more thorough treatment of the absorption lineshape should also be undertaken that includes the radial and propagation distance dependence of the laser inside the discharge.

Appendix A. Fraunhofer Diffraction Theory to Find Slit Width

The slit width of the spectrometer needed to be known, but was not of great importance. The experiments in this thesis that used the spectrometer were not dependent upon resolution because all of the lineshapes were integrated over before any data were analyzed. Instead, it was decided that having a greater signal throughput was more important. Knowing the entrance slit width of the spectrometer would allow the width to be set so that the resolution on the PI-MAX iCCD was good enough to resolve the transition lines, but also so the maximum amount of light made it through the spectrometer. To calibrate the spectrometer slit width, a 543.5 nm derivate of a standard HeNe laser was shined through the slit and onto an imaging screen 0.756 m away from the slit, as shown in Figure 30.

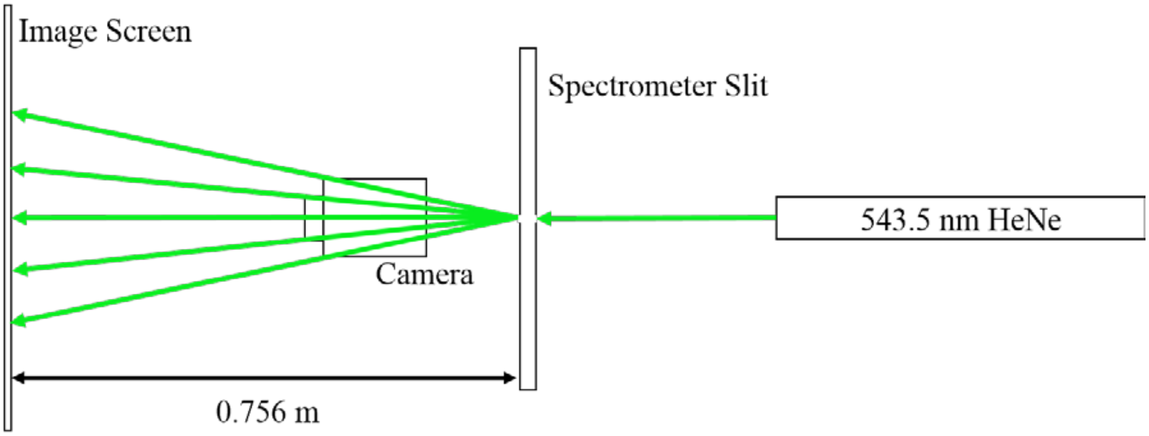

Figure 30. A 543.5 nm HeNe laser was incident upon the spectrometer slit and diffracted onto an image screen. A Nikon D50 SDLR camera was placed below the beam path and angled upward so that pictures of the diffraction pattern could be taken.

Photographs of the resulting diffraction pattern were taken with a Nikon D50 SDLR of each micrometer position from 0.25 to 0.01 in steps of 0.01. After loading the pictures onto a computer, the picture files were converted from Nikon's proprietary .NEF type to .jpeg. The .jpg file type was chosen because that was the conversion software readily available and the markings on the micrometer dial were expected to be similar to the actual slit width, so using a lossy file conversion was not anticipated to be an issue. The .jpeg pictures were loaded into a self-developed MATLAB® file that used single slit Fraunhofer diffraction theory to calculate the spectrometer slit width. An example of a Fraunhofer diffraction pattern is shown in Figure 31.

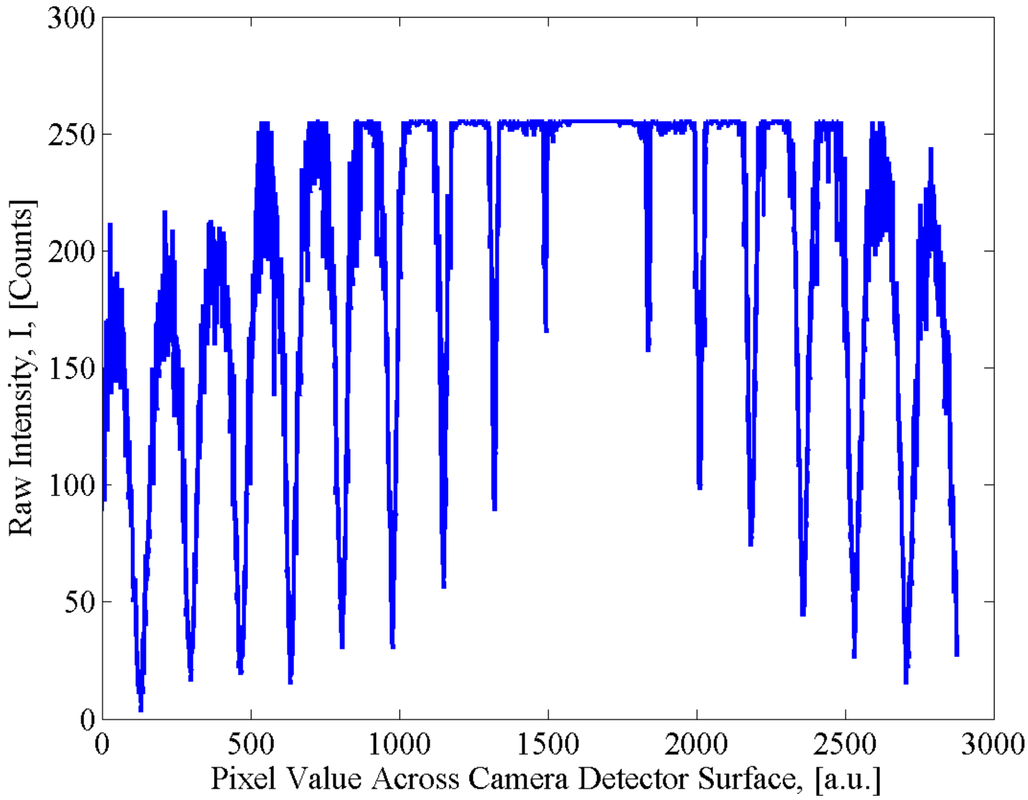

Figure 31. Example of a Fraunhofer diffraction pattern. This pattern, as well as many other patterns like this, were used to find the spectrometer slit width. The pattern ideally has rounded peaks, but this pattern does not because of noise inherent to the detector and saturation of the detector pixels.

The formula that predicts where a minimum, also known as a dark fringe, in the intensity pattern occurs is

$$m\pi = \frac{kb}{2}\sin\theta \tag{16}$$

where *m* is the order of the fringe, *k* is the wavenumber of the light that created the diffraction pattern, *b* is the width of the slit the light is incident on, and *θ* is the angular spread of the fringe [16]. The angular spread of the fringe was found as

$$\sin\theta = \frac{x}{\sqrt{x^2 + y^2}} \tag{17}$$

where *x* is the distance from the center of the dark fringe under observation to the center of the zero-order, or center-most, bright fringe, and *y* is the distance from the slit to the image plane. Solving Equation (8) for *b*, substituting in Equation (9), and using the relation $k=2\pi/\lambda$, the slit width is found as

$$b = \pm m\lambda \frac{\sqrt{x^2 + y^2}}{x}. \tag{18}$$

Using this formula and intensity patterns similar to the one shown in Figure 19, it was found that a 0.01 increase in micrometer position corresponded to a 10 µm increase in slit width. By knowing this, the entrance slit on the spectrometer was able to be set at 100 µm.

Appendix B. Calibration of PI-MAX2 with a Quartz Tungsten Halogen Lamp

Calibration of the PI-MAX iCCD was accomplished by finding the detectivity of the iCCD array. The method of doing this for any detector is to experimentally acquire a spectrum from a source with a well-known intensity curve and compare that to the theoretical curve. This is typically done with a small-area blackbody, but the blackbody available was not bright enough to be seen above the noise inherent to the detector using the experimental integration time. An Oriel Instruments 200 Watt quartz tungsten halogen (QTH) lamp was used instead. This particular lamp had a given spectrum of

$$E(\lambda) = \lambda^{-5} * \exp\left[42.98953 - \frac{4583.98173}{\lambda}\right] * \\ \left(.95373275 - \frac{56.503078}{\lambda} + \frac{211819.74}{\lambda^2} - \frac{1.423255\times10^{8}}{\lambda^3} + \frac{3.847842\times10^{10}}{\lambda^4} - \frac{3.8965903\times10^{12}}{\lambda^5}\right), \quad (19)$$

where $E(\lambda)$ is the spectral irradiance with units of mW/m^2-nm and λ is the wavelength in nanometers. By multiplying this irradiance by the detector area, which can be taken as the area of the focusing optic in front of the fiber optic, the spectral power, $\phi(\lambda)$, was found. The detectivity was then found as

$$D(\lambda) = \frac{QTHData}{t_{QTH}} \times \frac{1}{\phi(\lambda)} \times res_{pix}\,, \quad (20)$$

where $D(\lambda)$ is the spectral detectivity in intensity counts on the iCCD per Joule, $QTHData$ is the experimental data acquired for the quartz halogen lamp in intensity counts per pixel, t_{QTH} is the integration time of the data acquisition in seconds, and res_{pix} is the pixel-wavelength resolution in pixels per nanometers. This detectivity value was then averaged over 0.17561 nm, centered on the center of each transition wavelength provided in Section 2.1. There was significant variation in the calculated detectivity as a function of wavelength. This was caused by the noise present within the QTH data and it would have incorrectly influenced the experimental data had it been used without averaging. With the detectivity known, the number of photons detected during an experiment could be found. It is easiest to show this process with the QTH lamp data first. To recover the spectral power emitted by the QTH lamp, Eq. [Detectivity] is solved for $\phi(\lambda)$,

$$\phi(\lambda) = \frac{QTHData}{t_{QTH}} \times \frac{1}{D(\lambda)} \times res_{pix} \, . \tag{21}$$

Minor manipulation of Equation (13) is required to adapt this equation for other experiments. *QTHData* would be replace by the data from that particular experiment, and the integration times of the data acquisitions would become the ratio $t_{QTH}/t_{experimental}$. The ratio of the solid angle subtended by each detector,

$$Ratio\ of\ \ Solid\ \ Angle\ Subtended = \frac{A_{QTHD}}{A_{eD}} \left(\frac{r_{ep}}{r_{QTH}} \right)^2 , \tag{22}$$

where A_{QTHD} is the detector area used to collect the QTH lamp data, A_{eD} is the area used to collect the experimental data, r_e is the distance between the source and the optic for the experiment, and r_{QTH} is the distance between the source and the optic when collecting the QTH lamp data, would also be multiplied into Equation (13).

To collect the experimental spectrum from the QTH lamp, the same fiber optic used for the OES experiment was used. The fiber optic viewing angle was centered on the QTH lamp and the optic itself was placed a distance of 8 cm away and on the same horizontal plane as the center of the lamp. The distance of 8 cm, as opposed to the recommended 50 cm distance, was used so that enough signal was gathered within the OES experimental integration time of 100 ms to form a clear intensity curve. While the data did appear noisy, as referenced above, an overarching behavior of a curve was present. By using a distance of 8 cm, Equation (11) had to be multiplied by $(50/8)^2$. This was due to the irradiance of a Lambertian light source, which the lamp was assumed to be, dropping off as $1/r^2$, where r is the distance between the source and the detector. Data was taken for every transition line in Table 1. After all data was taken, the process to find detectivity discussed above was used.

Appendix C. Spectra for Each Transition Line Under Investigation

The spectral lines are shown below in the order they appear on Table 1, except the 727 nm line. The two transition lines near 772 nm are shown on the same plot. All plots follow the same convention as Figure 11: blue represents unpumped data, red represents pumped data, asterisks indicate the spectra for a pressure of 0 Torr, squares for 100 Torr, diamonds for 400 Torr, and circles for 700 Torr.

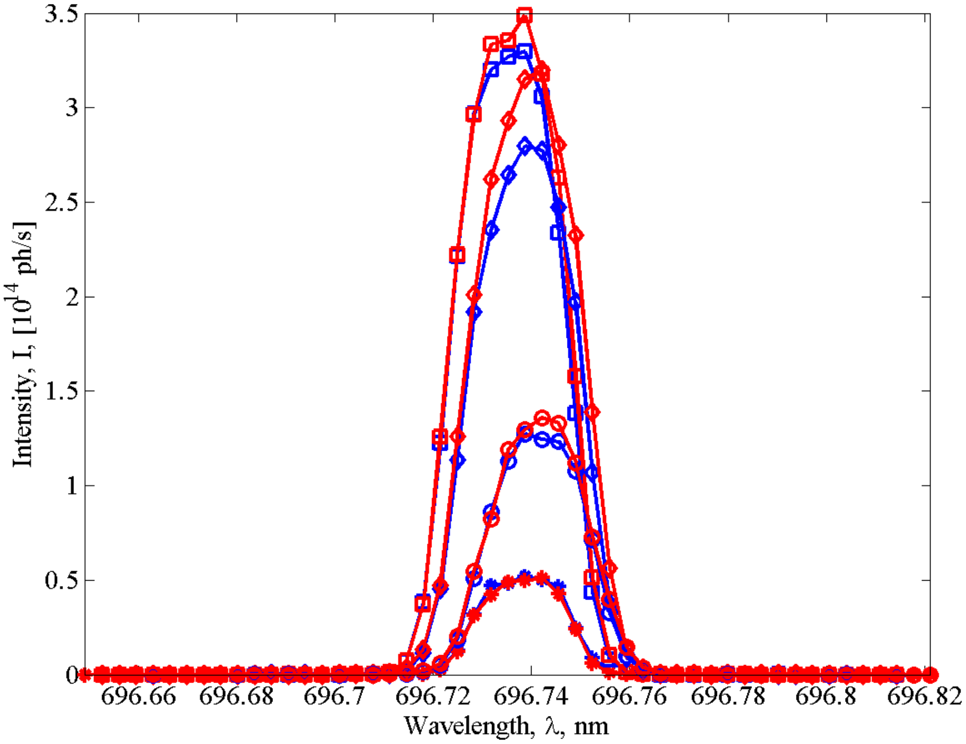

Figure 32. Spectra collected of the 696 nm line at all pressures.

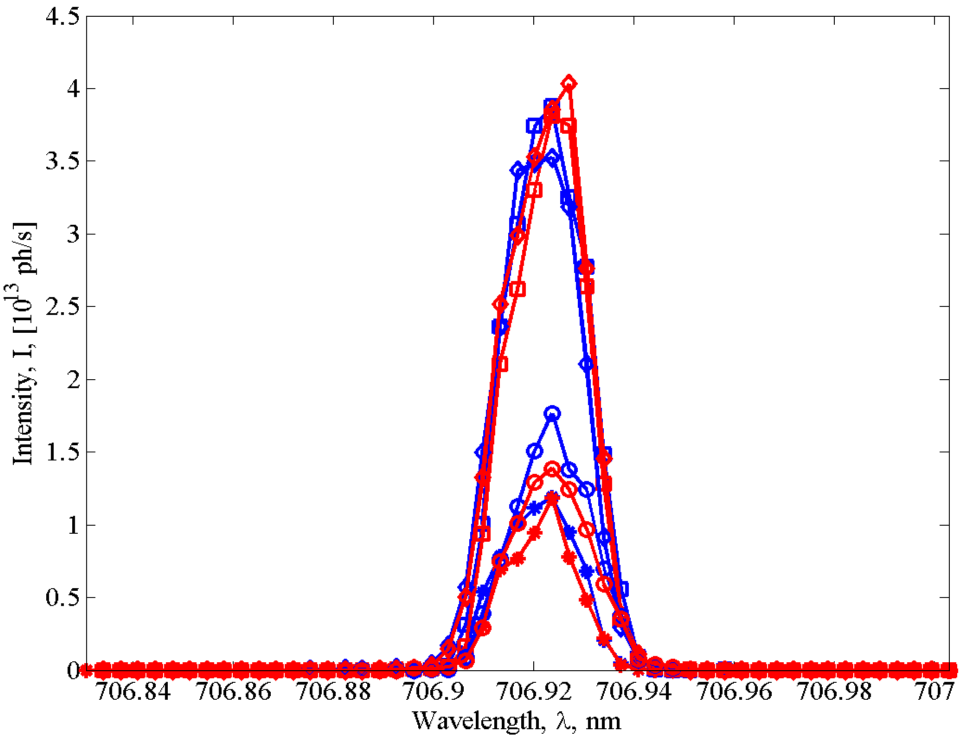

Figure 33. Spectra collected of the 706 nm line at all pressures.

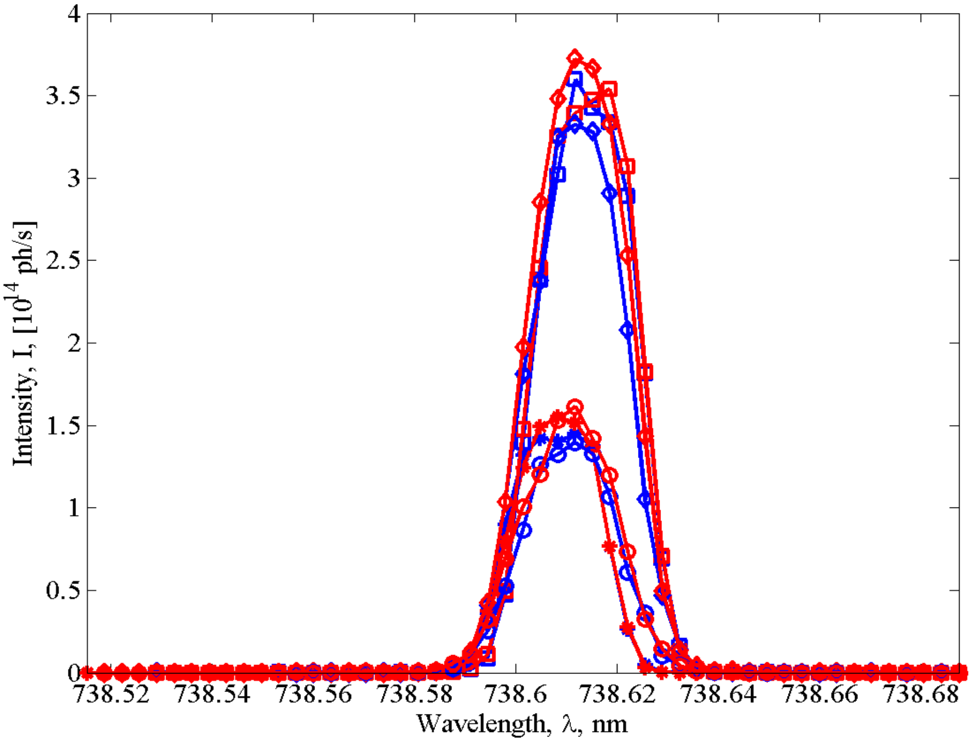

Figure 34. Spectra collected of the 738 nm line at all pressures.

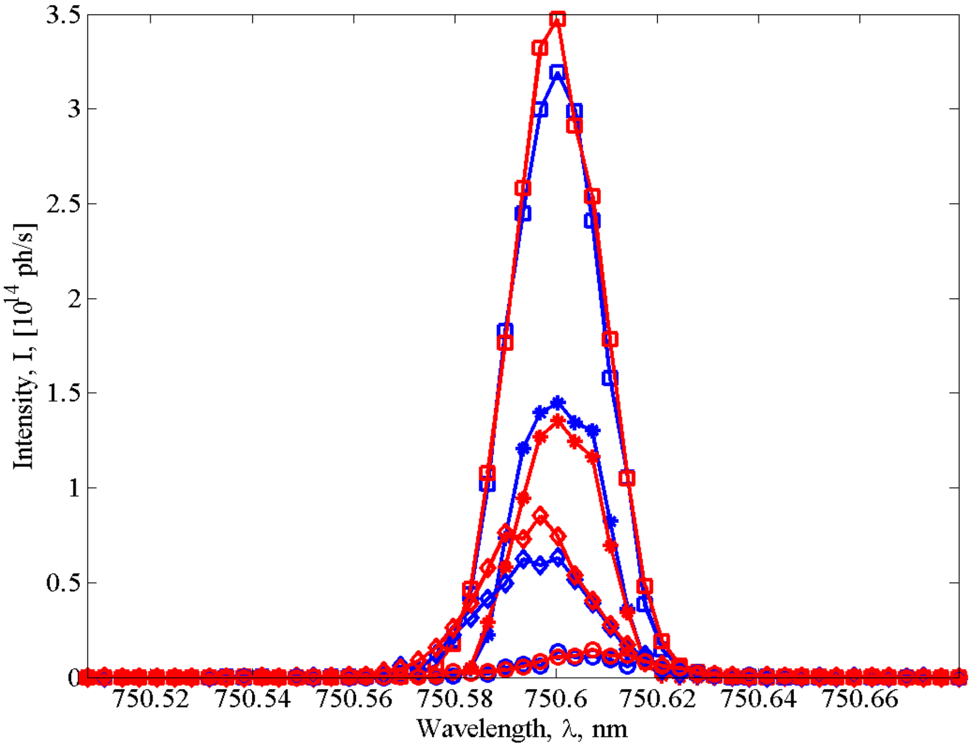

Figure 35. Spectra collected of the 750 nm line at all pressures.

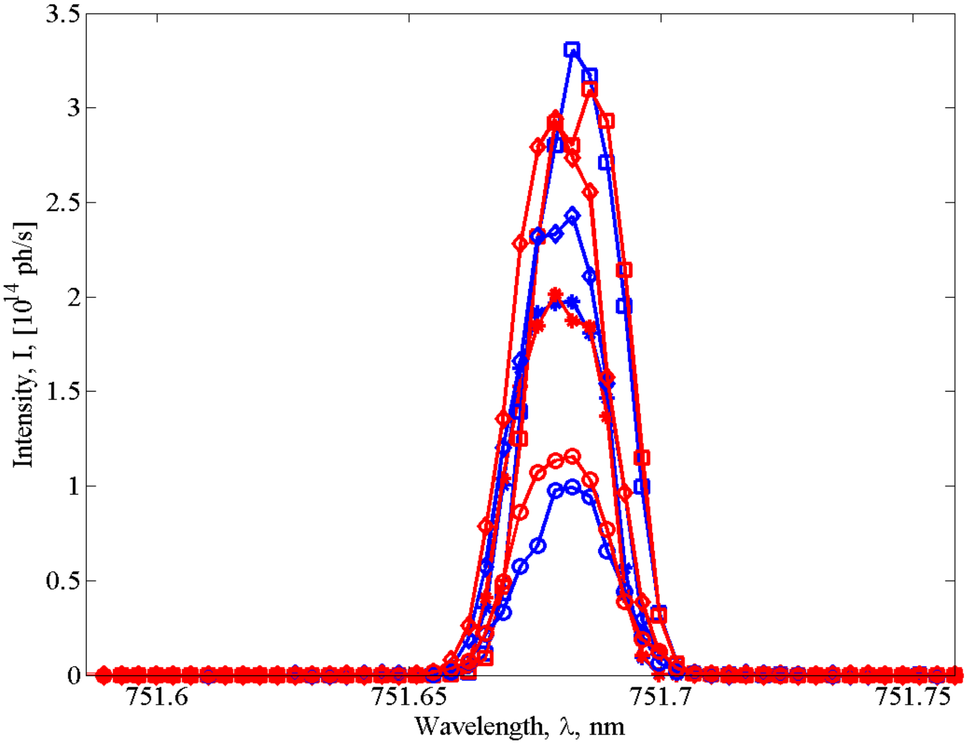

Figure 36. Spectra collected of the 751 nm line at all pressures.

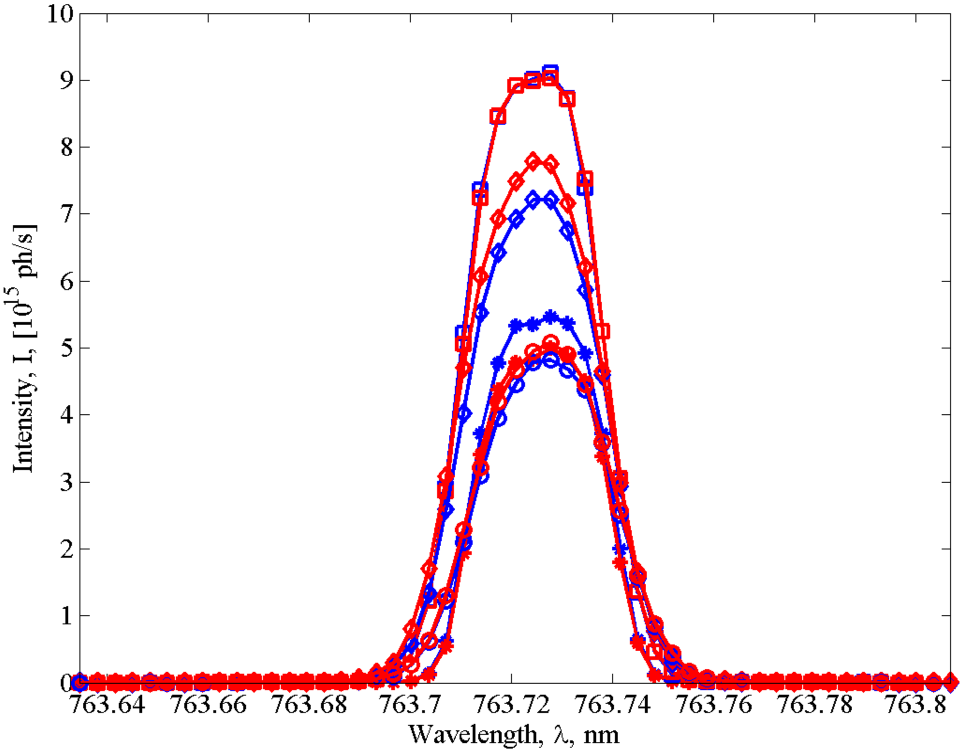

Figure 37. Spectra collected of the 763 nm line at all pressures.

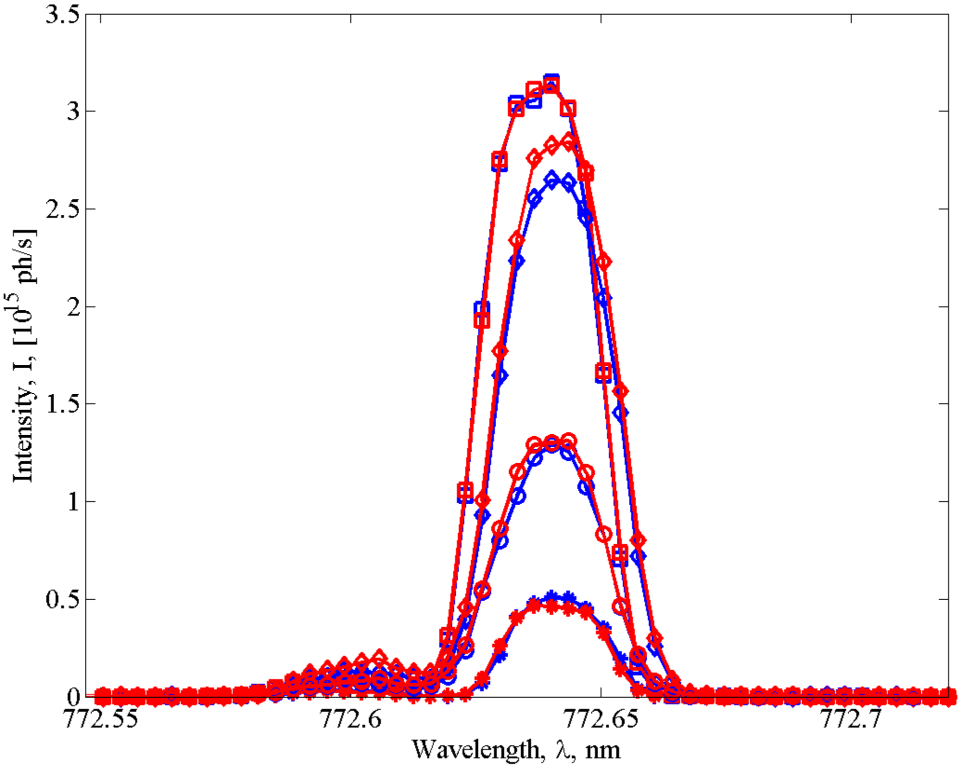

Figure 38. Spectra collected of the 772 nm lines at all pressures.

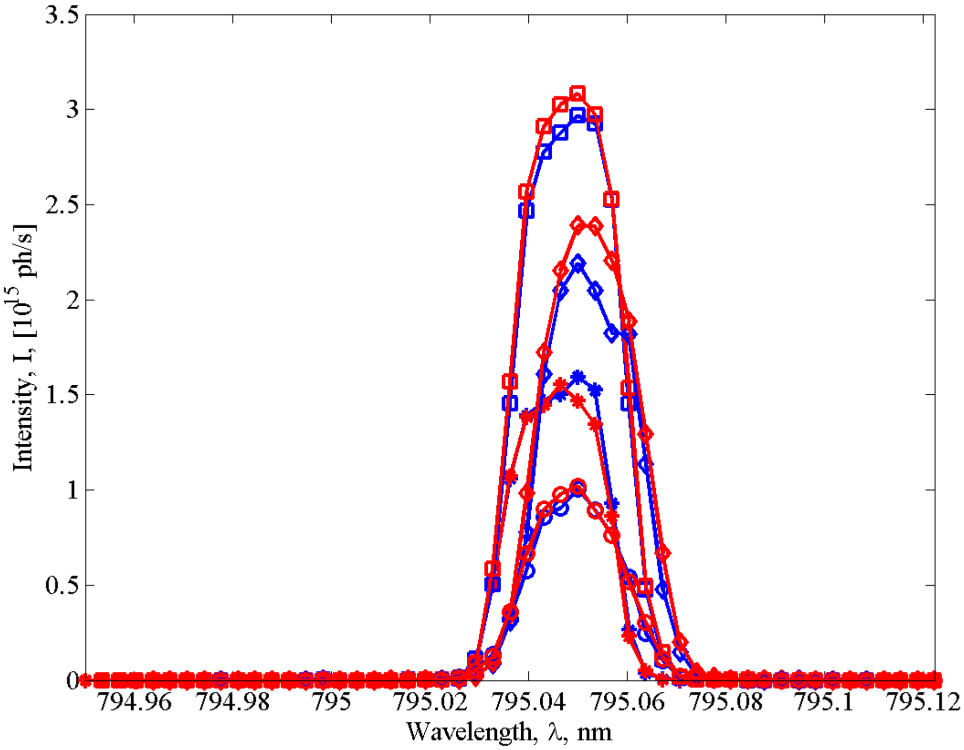

Figure 39. Spectra collected of the 795 nm line at all pressures.

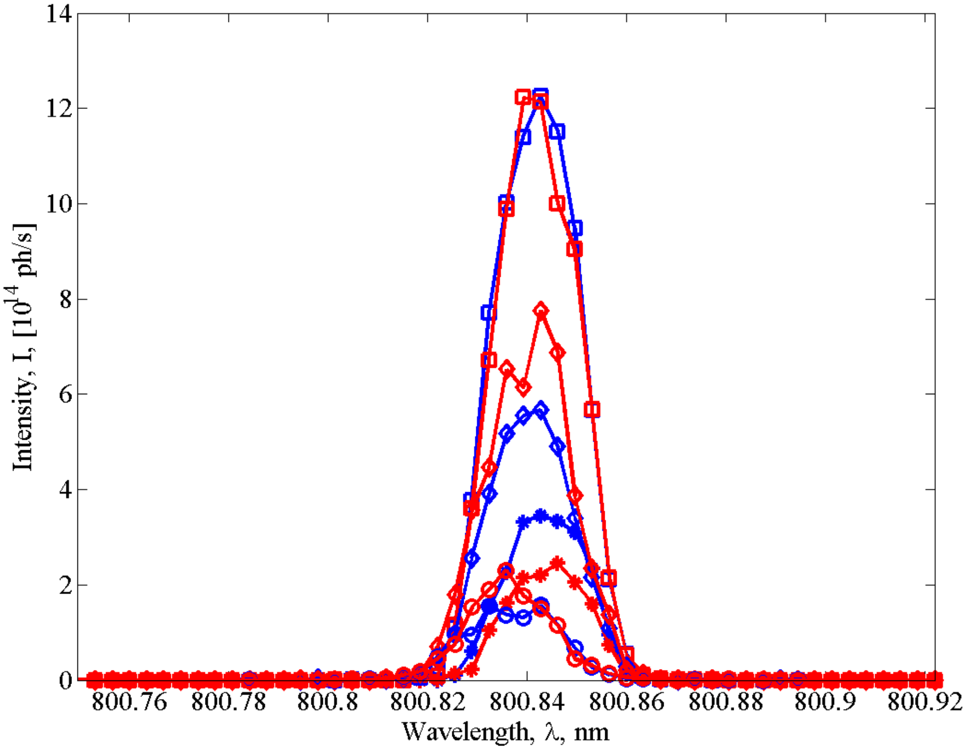

Figure 40. Spectra collected of the 800 nm line at all pressures.

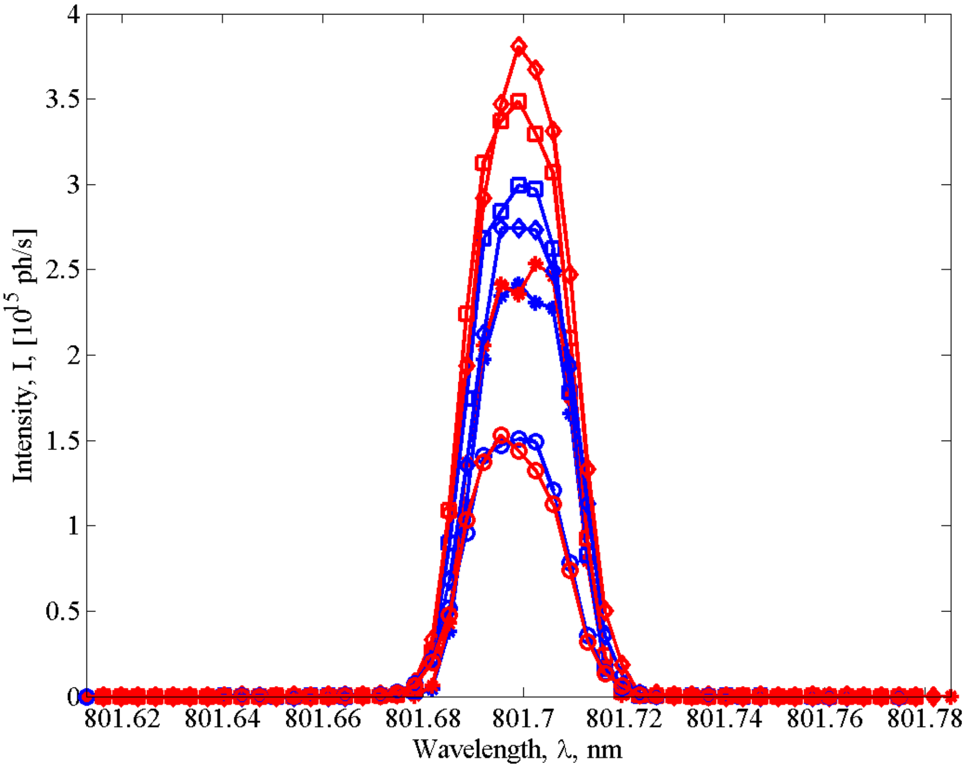

Figure 41. Spectra collected of the 801 nm line at all pressures.

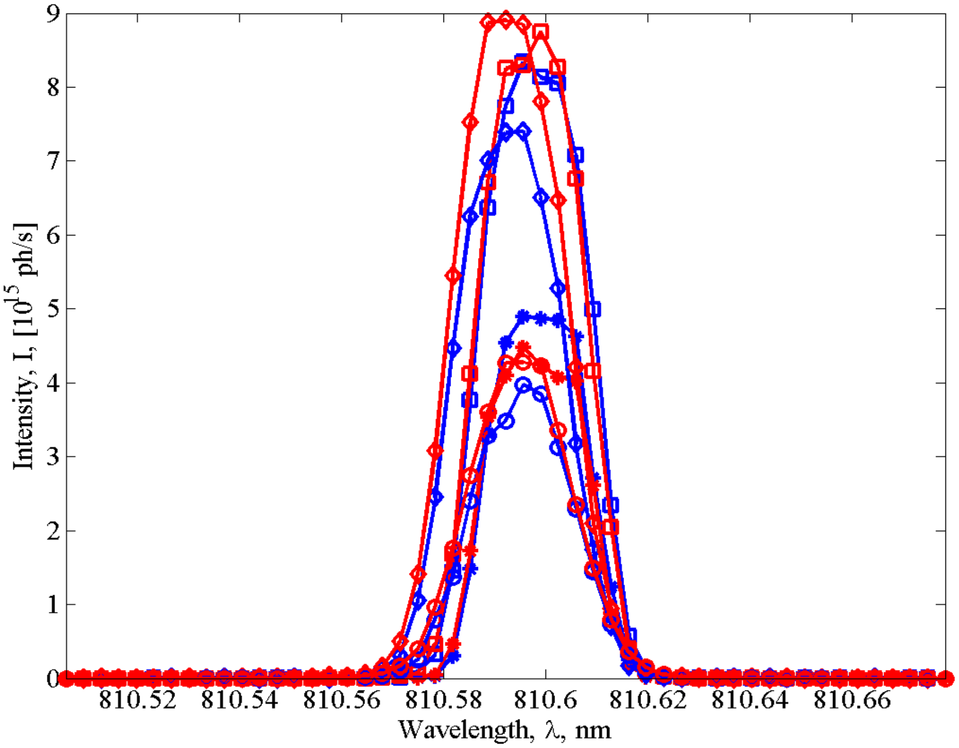

Figure 42. Spectra collected of the 810 nm line at all pressures.

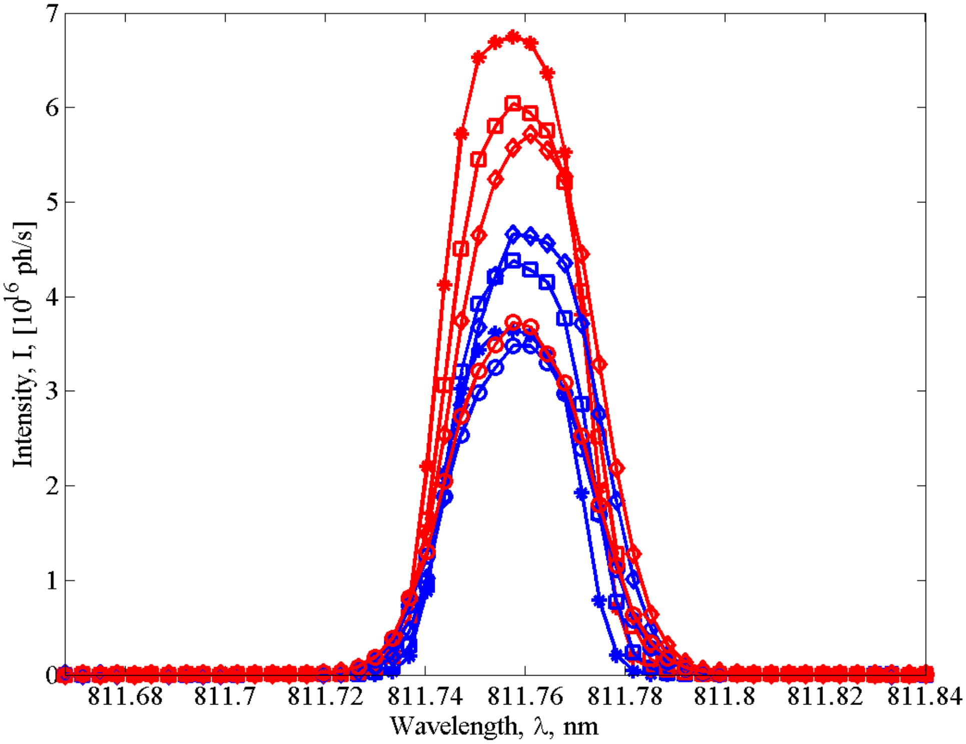

Figure 43. Spectra collected of the 811 nm line at all pressures.

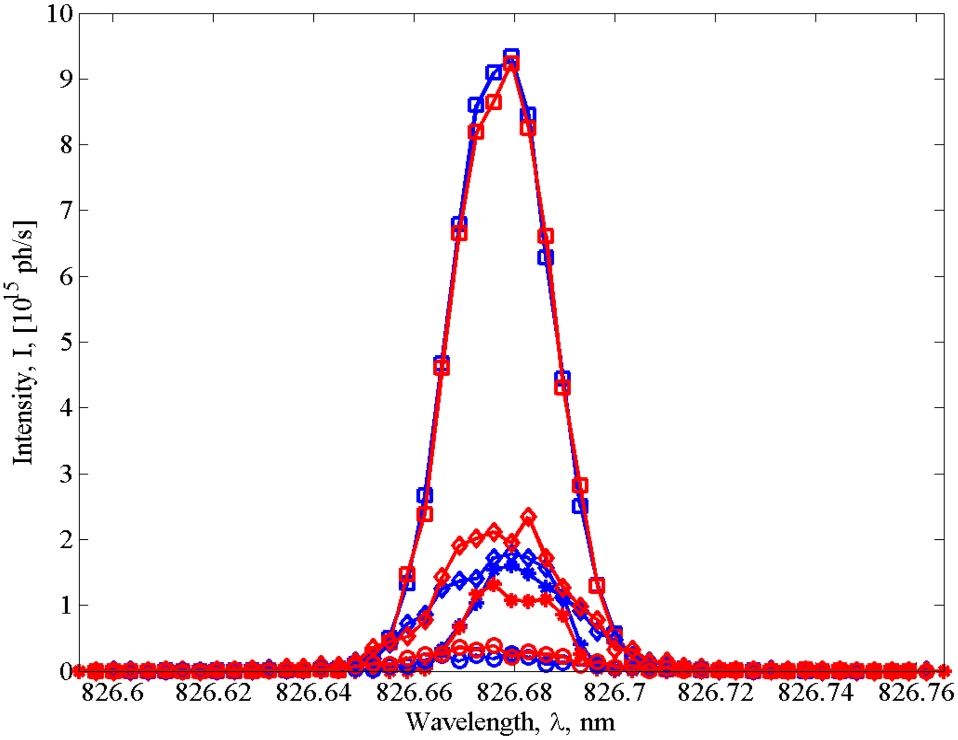

Figure 44. Spectra collected of the 826 nm line at all pressures.

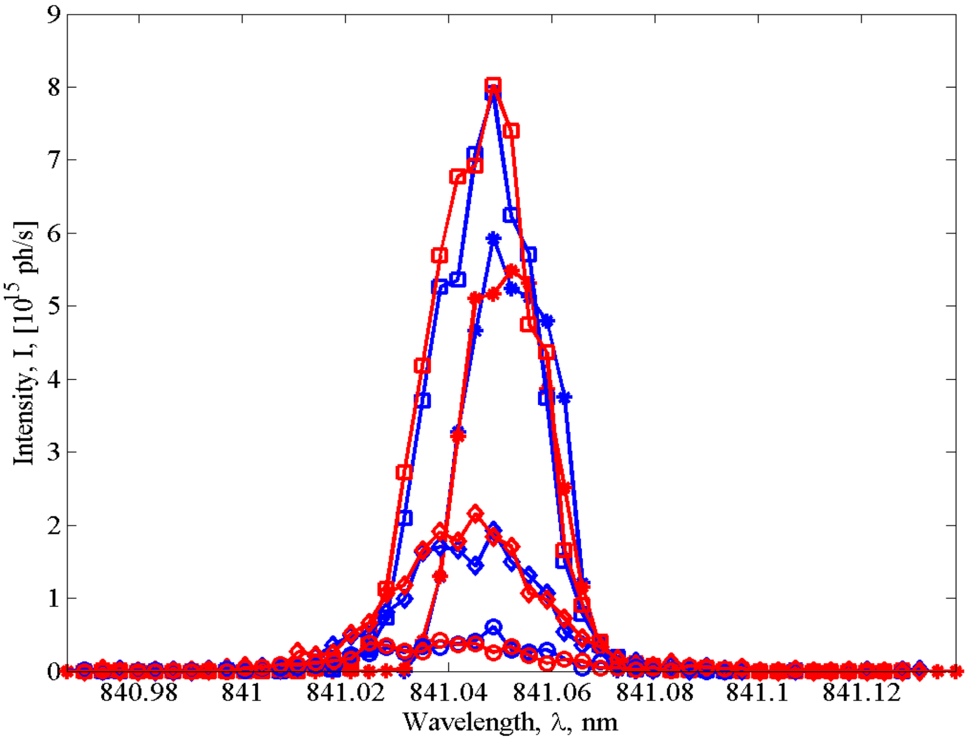

Figure 45. Spectra collected of the 841 nm line at all pressures.

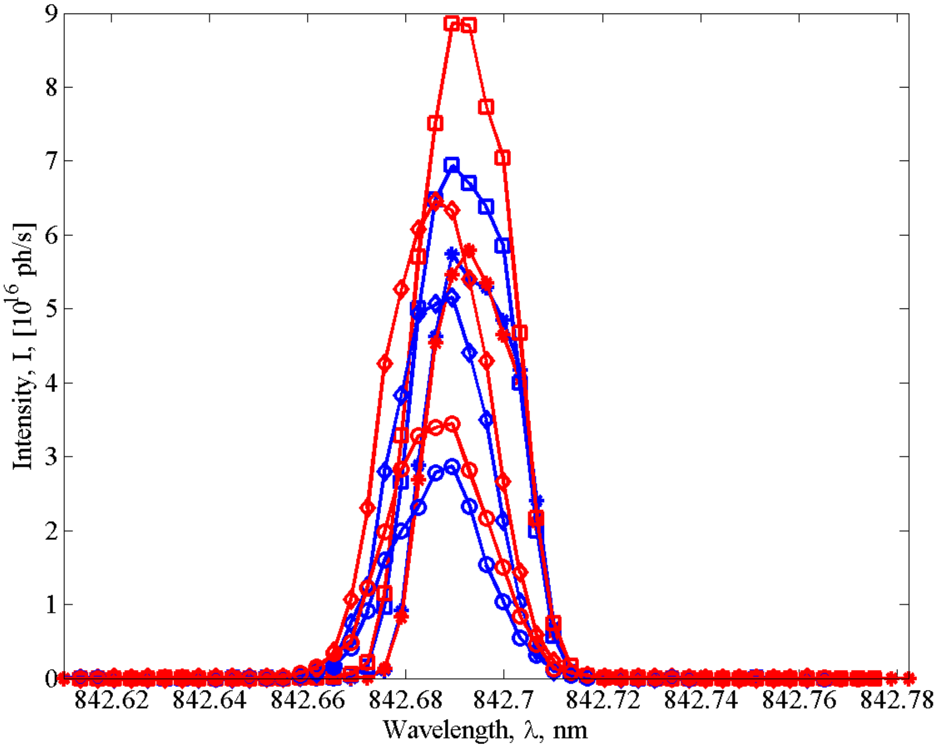

Figure 46. Spectra collected of the 842 nm line at all pressures.

Bibliography

1. Dickerson, Robert A. Chemical Oxygen Iodine Laser. Rockwell International Corporation, assignee. Patent US4780880A. 25 Oct. 1988. Print.

2. Krupke, William F. Diode-Pumped Alkali Laser. William F. Krupke, assignee. Patent US6643311 B2. 04 Nov. 2003. Print

3. Krupke, William F. “Diode pumped alkali lasers (DPALs) – A review (rev1)”. *Progress in Quantum Electronics*, 36:4-28, 2012.

4. Pitz, G. and P. Moran. “Advancements in flowing diode pumped alkali lasers”. *SPIE Proceedings*, 2016.

5. Han, J. and M. Heaven. “Gain and lasing of optically pumped metastable rare gas atoms”. *Optics Letters*, 37:11:2157-2159, 2012.

6. Tam, A., G. Moe, and W. Happer. “Particle formation by resonant laser light in alakali-metal vapor”. *Physical Review Letters*, 35:1630, 1975.

7. Norlén, G. “Wavelengths and energy levels of Ar I and Ar II based on new interferometric measurements in the region 3400-9800 Å”. *Phys. Scr*, 8:249-268, 1973.

8. Katori, H. and F. Shimizu. “Lifetime measurement of the $1s_5$ metastable state of argon and krypton with a magneto-optical trap", *Physical Review Letters*, 70:23:3545-3548, 1993.

9. Rawlins, W.T., et. al. “Laser excitation dynamics of argon metastables generated in atmospheric pressure flows by microwave frequency microplasma arrays”, *Proceedings of SPIE*, 8962:8962031-89620318, 2014.

10. Eshel, Ben. "Spectral analysis and metastable absorption measurements of high pressure capacitively and inductively coupled radio-frequency argon-helium discharges." Thesis. Air Force Institute of Technology, 2013. Print.

11. Han, J., et. al. “Demonstration of a diode-pumped metastable Ar laser”, *Optics Letters*, 38:24:5458-5461, 2013.

12. Rawlins, W.T., et. al. “Optically pumped microplasma rare gas laser”, *Optics Express*, 23:4:4804-4813, 2015.

13. Demtroder, Wolfgang. “Saturation of Inhomogeneous Line Profiles.” *Laser Spectroscopy*. Vol. 2. Berlin: Springer, 2008. 86-92. Print.

14. Tachibana, K., et. al. “Measurements of collisional broadening and shift of argon spectral lines using a tunable diode laser”, *Journal of Physics B: Atomic, Molecular and Optical Physics*, 15:3169-3178, 1982.

15. Nelson, C. and J. Crist. "Predicting Laser Beam Characteristics." *Laser Technolgy Journal*, 1:36-39, 2012.

16. Hecht, Eugene. “Diffraction.” *Optics*. 4th ed. San Francisco: Addison Wesley, 2002. 456. Print.

REPORT DOCUMENTATION PAGE	*Form Approved* *OMB No. 074-0188*

1. REPORT DATE *(DD-MM-YYYY)* 24-03-2016	**2. REPORT TYPE** Master's Thesis	**3. DATES COVERED** *(From – To)* Oct 2014 – March 2016

TITLE AND SUBTITLE POPULATION DENSITY MEASUREMENTS OF THE EXCITED STATES OF AN OPTICALLY EXCITED ARGON DISCHARGE USING EMISSION AND ABSORPTION SPECTROSCOPY	**5a. CONTRACT NUMBER** **5b. GRANT NUMBER** **5c. PROGRAM ELEMENT NUMBER**
6. AUTHOR(S) Owens, Steven A., 2nd Lieutenant, USAF	**5d. PROJECT NUMBER** **5e. TASK NUMBER** **5f. WORK UNIT NUMBER**
7. PERFORMING ORGANIZATION NAMES(S) AND ADDRESS(S) Air Force Institute of Technology Graduate School of Engineering and Management (AFIT/ENP) 2950 Hobson Way, Building 640 WPAFB OH 45433-8865	**8. PERFORMING ORGANIZATION REPORT NUMBER** AFIT-ENP-12-M-078
9. SPONSORING/MONITORING AGENCY NAME(S) AND ADDRESS(ES) High Energy Laser Joint Technology Office 801 University Blvd. SE, Suite 209 Albuquerque, NM 87106 Phone: 505-248-8208 Email: harro.ackermann@jto.hpc.mil	**10. SPONSOR/MONITOR'S ACRONYM(S)** HEL JTO **11. SPONSOR/MONITOR'S REPORT NUMBER(S)**

12. DISTRIBUTION/AVAILABILITY STATEMENT
DISTRUBTION STATEMENT A. APPROVED FOR PUBLIC RELEASE; DISTRIBUTION UNLIMITED.

13. SUPPLEMENTARY NOTES
This material is declared a work of the U.S. Government and is not subject to copyright protection in the United States.

14. ABSTRACT

The populations of the excited argon $3s^23p^54s$ (s5 only) and $3s^23p^54p$ configurations in a 10 W radio frequency discharge has been studied using optical emission and diode laser absorption spectroscopy. By optically bleaching the s5→p9 transition with a narrow band laser pump of about 10 W/cm^2 at 811 nm, the p9 population was increased by about a factor of 2 at a pressure of 5 Torr. At higher pressure, collisional mixing to adjacent p-states limited the laser-increased p9 population to less than 10 percent. All other laser-induced p-state populations were minimally affected at low pressure and increased by about a factor of 4 at higher pressure. The low pressure absorption line shapes exhibited an inhomogeneous hole with band-integrated absorbance that scaled linearly with pump power. The s5 population was greater than 7×10^{11} cm^{-3} at a pressure of 5 Torr, and about 57 percent of this population was moved to the p9 state at 828 mW, or about 10 W/cm^2. Implications for development of a higher power optically pumped rare gas laser are discussed.

15. SUBJECT TERMS
Rare Gas Laser, Optical Excitation Spectroscopy, Tunable-Diode Laser Absorption Spectroscopy

16. SECURITY CLASSIFICATION OF:			**17. LIMITATION OF ABSTRACT**	**18. NUMBER OF PAGES**	**19a. NAME OF RESPONSIBLE PERSON** Dr. Glen P. Perram, AFIT/ENP
a. REPORT	**b. ABSTRACT**	**c. THIS PAGE**			**19b. TELEPHONE NUMBER** *(Include area code)*
U	U	U	U	90	(937) 255-3636, x4504; (Glen.Perram@afit.edu)

Standard Form 298 (Rev. 8-98)
Prescribed by ANSI Std. Z39-18